1 **Revisiting the trend in the occurrences of the "warm Arctic-cold Eurasian continent"**

2 **temperature pattern**

3 Lejiang Yu[1,2]*, Shiyuan Zhong[3], Cuijuan Sui[4] , and Bo Sun[1]

4 1MNR Key Laboratory for Polar Science, Polar Research Institute of China, Shanghai, China

5 2 Southern Marine Science and Engineering Guangdong Laboratory (Zhuhai), Zhuhai, Guangdong,

6 China

7 3Department of Geography, Environment and Spatial Sciences, Michigan State University, East

8 Lansing, MI, USA

9 4 National Marine Environmental Forecasting Center, Beijing, China

10

11 *Corresponding Author's address

12 Dr. Lejiang Yu

13 MNR Key Laboratory for Polar Science, Polar Research Institute of China

14 451 Jinqiao Rd. Shanghai, 200136

15 Phone: 86-21-58712034,

16 Email: yulejiang@sina.com.cn

17

18

19

20

21

22

Abstract. The recent increasing trend of "warm Arctic, cold continents" has attracted much attention, but it remains debatable as to what forces are behind this phenomenon. Here, we revisited surface-temperature variability over the Arctic and Eurasian continent by applying the Self-Organizing-Map (SOM) technique to gridded daily surface temperature data. Nearly 40% of the surface temperature trends are explained by the nine SOM patterns that depict the switch to the current warm Arctic-cold Eurasia pattern at the beginning of this century from the reversed pattern that dominated the 1980s and the 90s. Further, no cause-effect relationship is found between the Arctic sea-ice loss and the cold spells in high-mid latitude Eurasian continent suggested by earlier studies. Instead, the increasing trend in warm Arctic-cold Eurasia pattern appears to be related to the anomalous atmospheric circulations associated with two Rossby wavetrains triggered by rising sea surface temperature (SST) over the central North Pacific and the North Atlantic Oceans. On interdecadal timescale, the recent increase in the occurrences of the warm Arctic-cold Eurasia pattern is a fragment of the interdecadal variability of SST over the Atlantic Ocean as represented by the Atlantic Multidecadal Oscillations (AMO), and over the central Pacific Ocean.

1   Introduction

In recent decades, winter season temperature in the Arctic has been rising at a rate faster than the warming experienced in any other regions of the world (Stroeve et al., 2007; Screen and Simmonds, 2010; Stroeve, 2012). In contrasts, there has been an increasing trend in colder than normal winters over the northern mid-latitude continents (Mori et al., 2014; Cohen et al., 2014; 2018). This pattern of opposite winter temperature trend between the Arctic and high-mid latitude continents, referred to as the warm Arctic-cold continents pattern (Overland et al., 2011; Cohen et al., 2014; Walsh, 2014), has received considerable interest in the scientific community especially with regard to dynamical and physical mechanisms for the development of the phenomenon (Mori et al., 2014;Vihma, 2014; Barnes and Screen, 2015; Kug et al., 2015; Overland et al., 2015; Chen et al., 2018).

Using observational analyses or coupled ocean-atmosphere modeling, a number of studies have attributed the recent warm Arctic-cold continents pattern to the Arctic sea ice loss in boreal winter (Inoue et al., 2012; Tang et al., 2013; Mori et al., 2014; Kug et al., 2015; Cohen et al., 2018; Mori et al., 2019). Sea ice variability in different parts of the Arctic Ocean has been linked to climate variability in different parts of the world. Specifically, sea ice loss in the Barents and Kara Seas has been linked to cold winters over East Asia (Kim et al., 2014; Mori et al., 2014; Kug et al., 2015; Overland et al., 2015) and in central Eurasia (Mori et al., 2014), while a similar connection has been found between cold winters in North America and sea ice retreat in the East Siberian and Chukchi Seas (Kug et al., 2015). A most recent study (Matsumura and Kosaka, 2019) attributed the warm Arctic-cold continents pattern to the combined effect of Arctic sea ice loss and the atmospheric teleconnection induced by tropical Atlantic sea-surface temperature (SST) anomalies.

Other studies, however, found no cause-and-effect relationship between Arctic sea ice loss and

67 mid-latitude climate anomalies (Blackport et al., 2019; Fyfe, 2019). Numerical modeling studies using

68 coupled ocean and atmospheric models simulated no cold mid-latitude winters when the models were

69 forced with reduced Arctic sea ice cover (McCusker et al., 2016; Sun et al., 2016; Koenigk et al., 2019;

70 Blackport et al., 2019; Fyfe, 2019). Instead, these studies pointed to internal atmospheric variability as

71 the likely cause for cold winters in mid-latitudes. Some studies have also suggested that on the

72 interannual timescale mid-latitude atmospheric circulation anomalies triggered by the Pacific and

73 Atlantic SST oscillations may explain both the Arctic sea ice loss and the cooling of the high-mid

74 latitudes (Lee et al., 2011; Luo et al., 2016; Peings et al., 2019; Matsumura and Kosaka, 2019; Clark

75 and Lee, 2019). The sea surface temperature anomalies over the Gulf Stream have also been linked to

76 the Barents Sea ice loss and Eurasian cooling (Sato et al., 2014).

77   Despite the recent attention given to the warm Arctic-cold continents pattern, it remains debatable

78 as to the roles of various dynamical and physical processes play in the formation of this phenomenon.

79 In this study, we revisit surface temperature variability over the Arctic and Eurasia continent (40-90 $^\circ$N,

80 20-130 $^\circ$E), where the warm Arctic-cold continents pattern is a prominent feature (Cohen et al., 2014;

81 Mori et al., 2014), by applying the Self-Organizing-Map (SOM) technique to daily surface temperature

82 over the recent four decades. We will show that while the warm Arctic-cold Eurasian continent pattern

83 has dominated the recent two decades, its opposite pattern, cold Arctic-warm Eurasia continent,

84 appeared frequently in the 1980s and the 90s. Using century-long data, we will further show that the

85 warm Arctic-cold Eurasian continent pattern is an intrinsic climate mode and the recent increasing

86 trend in its occurrence is a reflection of an interdecadal variability of the pattern. Using linear

87 regression, we explain the reason for the recent increasing occurrences of the warm Arctic-cold

88 continents pattern. We also assess the role of the SST anomalies over the North Pacific and Atlantic

89   Oceans in the variability of the warm Arctic-cold Eurasia pattern on the interdecadal time scale.

90   **2   Datasets and methods**

91   2.1 Datasets

92   Daily surface air temperature and other climate variables used in the current analyses, including

93   500 hPa geopotential height, 800-hPa wind and mean sea level pressure, all come from the European

94   Centre for Medium-Range Weather Forecasts Re-Analysis (ERA), the interim version (ERA-Interim;

95   Dee et al., 2011) with a horizontal resolution of approximately 79 km (T255) and 60 vertical levels in

96   the atmosphere. Compared to the earlier versions of ERA (e.g., ERA-40, Uppala et al., 2005) and other

97   global re-analysis products (e.g. the NCEP reanalysis, Kalnay et al., 1996), ERA-Interim has been

98   found to be more accurate in portraying the Arctic warming trend (Dee et al., 2011; Screen and

99   Simmonds, 2011) despite its known warm and moist bias in the surface layer (Jakobson et al., 2012).

100 Daily sea ice data are obtained from the U.S. National Snow and Ice data Center

101 (ftp://sidads.colorado.edu/DATASETS/nsidc0051_gsfc_nasateam_seaice/final-gsfc/north/daily).

102 Gridded monthly SST data used in the current analysis are obtained from the U.S. National Oceanic

103 and   Atmospheric   Administration   (NOAA)   data   archives

104 (ftp://ftp.cdc.noaa.gov/Datasets/noaa.oisst.v2.highres/) (Reynolds et al. 2007). In our analyses, we

105 remain the trends in the data over the 1979-2019 period.

106 The results obtained from the data within the recent four decades are put into the context of the

107 variability over longer time scales using data from the Twentieth Century Reanalysis project, version

108 2C (20CR) that spans more than a century from 1851 through 2015 (Compo et al., 2011). The 20CR

109 reanalysis data, which has a horizontal resolution of 2 °latitude by 2 °longitude and temporal resolution

110 of 6 hours, was produced by a model driven at the lower boundary by observed monthly SST and sea

111   ice conditions and with data assimilation of surface pressure observations. Several indices used to

112   describe known modes of climate variability including Arctic oscillation (AO), Northern Atlantic

113   Oscillation (NAO), Atlantic Multidecadal Oscillation (AMO) (Enfield et al., 2001) and PDO (Mantua

114   et al., 1997), are obtained from NOAA's Climate prediction Center (CPC)

115   (https://www.esrl.noaa.gov/psd/data/climateindices/list/),

116   2.2 Methods

117   From the perspective of nonlinear dynamic, a region's climate has its intrinsic modes of variability,

118   but the frequency of occurrence of these internal modes can be modulated by remote forces external to

119   the region (Palmer, 1999l; Hoskins and Woollings, 2015; Shepherd, 2016). In this study we will first

120   obtain the main modes of variability of wintertime surface temperature in a region (40-90 °N, 20-130 °E)

121   by applying the SOM method (Kohonen, 2001) to daily surface temperature data for the 40 winters

122   (December, January, February) from December 1979 through February 2019. The use of daily data

123   over four decades allows for capturing the variability across two time scales (synoptic and decadal).

124   SOM is a clustering method based on neural network that can transform multi-dimensional data into a

125   two-dimensional array without supervised learning. The array includes a series of nodes arranged by a

126   Sammon map (Sammon, 1969). Each node in the array has a vector that can represent a spatial pattern

127   of the input data. The distance of any two nodes in the Sammon map represents the level of similarity

128   between the spatial patterns of the two nodes. Because SOM has fewer limitations than most other

129   commonly used clustering methods, (e.g., orthorgonality required by the empirical orthogonal function

130   or EOF method), the SOM method can describe better the main variability patterns of the input data

131   (Reusch et al., 2005).

132   SOM method has been used in atmospheric research at mid and high latitudes of the northern

133 hemisphere (Skific et al., 2009; Johnson and Feldstein, 2010; Horton et al., 2015; Loikith and Broccoli,

134 2015; Vihma et al., 2019). For example, Johnson and Feldstein (2010) used SOM to identify spatial

135 patterns of daily wintertime North Pacific sea level pressure and relate the variability of the

136 occurrences of those patterns to some large-scale circulation indices. Loikith and Broccoli (2015)

137 compared observed and model-simulated circulation patterns across the North American domain using

138 an approaching involving SOM. The SOM method was also used to detect circulation pattern trends in

139 a subset of North America during two different periods (Horton et al., 2015).

140 In this study, the SOM method is applied to ERA-Interim wintertime daily temperature anomalies from

141 December 1979 through February 2019. The anomalies are calculated by subtracting 40-year averaged

142 daily temperature from the original daily temperature at each grid point. Prior to SOM analysis, it is

143 necessary to determine how many SOM nodes are needed to best capture the variability in the data.

144 According to previous studies (Lee and Feldstein, 2013; Gibson et al., 2017; Schudeboom et al., 2018),

145 the rule for determining the number of SOM nodes is that the number should be sufficiently large to

146 capture the variability of the data analyzed, but not too large to introduce unimportant details. Table 1

147 shows the averaged spatial correlation between all daily surface air temperature anomalies and their

148 matching nodes.   The spatial correlation coefficients increase from 0.26 for a 3×1 grid to 0.51 for a

149 4×4 grid, but the gain from a 3×3 grid to a 4×4 grid is relatively small. Hence, a 3×3 grid seems to

150 meet the above-mentioned rule and will be utilized in this study.

151   The contribution of each SOM node to the trend in wintertime surface temperature anomalies is

152 calculated by the product of each node pattern and its frequency trend normalized by the total number

153 (90) of wintertime days (Lee and Feldstein, 2013). The sum of the contributions from all nodes denotes

154 the SOM-explained trends. Residual trends are equal to the subtraction of SOM-explained trends from

155   the total trends. The anomalous atmospheric circulation pattern corresponding to each of the SOM

156   pattern is obtained by composite analysis that computes a composite mean of an atmospheric

157   circulation field (e.g., 500 hPa height) over all occurrences of that SOM node. Regression analysis is

158   also performed where atmospheric circulation variables are regressed onto the time series of the

159   occurrence of a SOM node to further elucidate the relationship between the variability of atmospheric

160   circulations and surface temperatures. The statistical significance of composite and regression analyses

161   in this study is tested by using the Student's t test.

162   **3   Results**

163   3.1 Surface temperature variability

164   The majority of the 9 SOM nodes depict a dipole pattern characterized by opposite changes in

165   surface temperatures between the Arctic Ocean and the Eurasian continent, although the sign switch

166   does not always occur at the continent-ocean boundary (Figure 1). The differences in the position of the

167   boundary between the warm and cold anomalies reflects the transition between the cold Arctic-warm

168   Eurasia pattern (denoted, in descent order of the occurrence frequency, by nodes 3, 9, 6), to the warm

169   Arctic-cold Eurasia pattern (depicted, in descent order of the occurrence frequency, by nodes 1, 7, 4).

170   The spatial patterns represented by the first group of nodes are almost mirror images of the patterns

171   denoted by the corresponding nodes in the second group. For example, the second node in group 1

172   (node 9, 15.4%) and the first node in group 2 (node 1, 17.1%) show a mirror image pattern with cold

173   (warm) anomalies in the Arctic Ocean extending into northern Eurasia and warm (cold) anomalies in

174   the rest of the Eurasia continent in the study domain. In both cases, the region of maximum magnitude

175   anomalies is centered near Svalbard, Norway. The second pair, denoted by node 3 (17.2%) and 7

176   (13.7%) has the boundary of separation moved northward from northern Eurasia continent toward the

177   shore of the Arctic Ocean. While the maximum anomaly in the Arctic Ocean remains close to Svalbard,

178   maximum values over the continent are found in central Russia. Nodes 4-6 display a noticeable

179   transition from node 1 to node 7 and from node 3 to node 9, respectively. Although nodes 2 and 8 show

180   an approximate monopole spatial pattern, they also represent a transition between nodes 1 and 3, and

181   between nodes 7 and 9, respectively. Above SOM analysis does not consider the trend in surface air

182   temperature. The result is similar when the trend is removed (not shown).

183   The temporal variability on this time scale is typically related to synoptic processes and hence the

184   questions are what synoptic patterns are responsible for the occurrence of the spatial patterns depicted

185   by each of the 9 SOM nodes and how these patterns are related to those of the Arctic sea ice anomalies?

186   These questions can be answered by using the composite method. Specifically, for each SOM node,

187   composite maps are made respectively for the anomalous 500-hPa geopotential height, mean sea level

188   pressure, 850-hPa wind, downward longwave radiation, surface turbulent heat flux, and sea ice

189   concentration over all the days when the spatial variability of the surface temperature anomalies is best

190   matched by the spatial pattern of that node.

191   3.2 Large-scale circulation patterns

192   For all SOM nodes, the spatial pattern of the composited 500-hPa geopotential height anomalies

193   (Figure 2) is similar to that of mean sea level pressure anomalies (not shown), indicating an

194   approximately barotropic structure. For nodes 1, 4 and 7, the 500-hPa height anomalies show a dipole

195   structure of positive values over Siberia and negative values to its south over the Eurasian continent.

196   Anomalous southwesterly winds on the western side of the anticyclone over Siberia transport warm

197   and moist air from northern Europe and the North Atlantic Ocean into the Atlantic sector of the Arctic

198   Ocean (Figure 3), providing a plausible explanation of the warm surface temperature anomalies in the

199   region (Figure 1). On the eastern side of the anticyclone, anomalous northwesterly winds bring cold

200   and dry air from the Arctic Ocean into Eurasia continent, which is consistent with the negative surface

201   temperature anomalies there. The opposite occurs for nodes 3, 6 and 9. A similar explanation involving

202   anomalous pressure and wind fields can be applied to other nodes. The dipole structure that dominates

203   the anomalous 500-hPa height fields over the North Atlantic Ocean for most nodes resembles the

204   spatial pattern of the NAO (Figure 2). In addition, the patterns for several nodes, such as nodes 4 and 7,

205   have some resemblance to the spatial pattern of the AO over larger geographical region. The possible

206   connection to NAO and AO is further investigated by averaging the daily index values of NAO or AO

207   over all occurrence days for each node. The results (Table 2) show that nodes 1, 2, 3 (5, 8, 9)

208   correspond to a significant positive (negative) phase of the NAO index characterized by negative

209   (positive) height anomalies over Iceland and positive (negative) values over the central North Atlantic

210   Ocean. Association is also found between nodes 1, 2, 3, and 6 (5, 7, 8, and 9) and the positive (negative)

211   phases of the AO index.

212   3.3 Downward radiative fluxes

213   Besides the anomalous circulation patterns, anomalous surface radiative fluxes may also play a role in

214   shaping the spatial pattern of surface temperature variability. In fact, the spatial pattern of the mean

215   anomalous daily downward longwave radiation for an individual node (Figure 4) is in good agreement

216   with the spatial pattern of the surface temperature anomalies of that node. In other words, increased

217   downward longwave radiation is associated with positive surface temperature anomalies, and vice

218   versa. As expected from previous studies (e.g., Sedlar et al. 2011), there is a significant positive

219   correlation between downward longwave radiative fluxes and the anomalous total column water vapor

220   and mid-level cloud cover (not shown). The correlation to low- and high-level cloud cover is, however,

221 not significant (not shown). Most of the water vapor in both the Arctic and Eurasia is derived from the

222 North Atlantic Ocean, but the water vapor is transported into the Arctic by southwesterly flows and into

223 Eurasia by northwesterly winds. The anomalous shortwave radiation corresponding to each node (not

224 shown) is an order of magnitude smaller that of the longwave radiation anomalies and has a spatial

225 pattern opposite to that of the mid-level cloud cover and the longwave radiation anomalies.

226 3.4 Sea ice

227   The analyses presented above attempt to explain the spatial pattern of surface temperature

228 variability for each node from the perspective of anomalous heat advection and surface radiative fluxes.

229 As mentioned earlier, there has been a debate in the literature about the role played by the sea ice

230 anomalies in the Barents and Kara Seas in the development of the warm Arctic-cold Eurasia pattern.

231 Here, we examine the anomalous turbulent heat flux (Figure 5) and sea ice concentration (Figure 6) for

232 each node. Turbulent heat flux is considered positive when it is directed from the atmosphere

233 downward to the ocean or land surfaces. Thus, a positive anomaly indicates either an increase in the

234 atmosphere-to-surface heat transfer or a decrease in the heat transfer from the surface to the atmosphere.

235 The magnitude of anomalous turbulent heat flux is found to be comparable to that of anomalous

236 downward longwave radiation (Figure 4). For all nodes, the heat flux anomalies are larger over ocean

237 than over land (Figure 5). For node 1, positive turbulent heat flux anomalies occur mainly over the

238 Barents Sea, the western and central North Atlantic Ocean and the eastern North Pacific Ocean,

239 indicating an increase in heat transport from the air to the ocean due possibly to an increase in vertical

240 temperature gradient caused by warm air advection associated with anomalous circulation (Figures 2

241 and 3). The downward heat transfer results in sea ice melt in the Greenland Sea and the Barents Sea

242 (Figure 6). For node 4, the anomalous southerly winds over the Nordic Sea produce larger positive

243   turbulent heat flux anomalies (Figure 5). For node 7, the anticyclone is located more northwards, which

244   generates opposite anomalous winds between the Nordic and northern Barents Seas and the southern

245   Barents Sea and thus opposite turbulent heat flux anomalies that are consistent with the opposite sea ice

246   concentration anomalies in the two regions (Figure 5). For nodes 3, 6, and 9, the anomalous cold air

247   from the central Arctic Ocean flows into warm water in the Nordic and Barents Seas, producing

248   negative turbulent heat flux anomalies and positive sea ice concentration anomalies (Figures 5 and 6).

249   Sorokina et al. (2016) noted that turbulent heat flux usually peaks 2 days before changes in surface

250   temperature pattern occur. The pattern of the composited anomalous 500-hPa geopotential height,

251   turbulent heat flux and sea ice concentration 2 days prior to the day when the nodes occur (not shown)

252   is similar to the current-day pattern in Figures 2, 5, and 6. Our results support the conclusion of

253   Sorokina et al. (2016) and Blackport et al. (2019) that the anomalous atmospheric circulations lead to

254   the anomalous sea ice concentration in the Barents Sea.

255   3.5 Trends in wintertime surface temperature

256   The results above suggest that both the surface temperature anomaly patterns over the Arctic Ocean

257   and Eurasian continent and the sea ice concentration anomalies in the Nordic and Barents Seas can be

258   explained largely by changes in atmospheric circulations and the associated vertical and horizontal heat

259   and moisture transfer by mean and turbulent flows. Next, we assess the trends of wintertime surface

260   temperature and the contributions of the SOM nodes to the trends.

261   We first examine the time series of the accumulated number of days for each node in each winter

262   for the 1979-2019 period (Figure 7). The time series for nodes 1, 4, 6, and 9 exhibit variability on

263   interannual as well as decadal time scales. The occurrence frequency is noticeably larger after 2003

264   than prior to 2003 for nodes 1 and 4, and vice versa for nodes 6 and 9, and the difference between the

265 two periods is significant at 95% confidence level. Given the spatial patterns of these four nodes

266 (Figure 1), this indicates that the warm Arctic-cold Eurasia pattern occurred more frequently after 2003.

267 A linear trend analysis of the time series for each node (Table 3) reveals significant positive trends in

268 occurrence frequency for nodes 1 and 4 and significant negative trends for nodes 6 and 9, which agree

269 with the result from a previous study (Clark and Lee, 2019; Overland et al., 2015) that suggested an

270 increasing trend of the warm Arctic and cold Eurasia pattern.

271 These trends in the occurrence frequency of the SOM nodes contribute to the trends in the total

272 wintertime (DJF) surface temperature anomalies (Figure 8, top panel) that have significant positive

273 trends over the Arctic Ocean and in regions of Northern and Eastern Europe and negative, mostly

274 insignificant trends in Central Siberia. The contribution, however, varies from node to node (Figure 9).

275 Node 1 has the largest domain-averaged contribution of 18.7%, followed by its mirror node (node 9) at

276 10.1%. Nodes 4 and 6 account for 2.8% and 4.3% of the total trend, respectively. None of the

277 remaining nodes explain more than 2%. All nodes together explain 39.5% of the total trend in

278 wintertime surface air temperature. The spatial pattern of the SOM-explained trends (Figure 8, middle

279 panel) is similar to the warm Arctic-cold continent pattern, whereas the residual trend resembles more

280 the total trend (Figure 8 bottom panel).

281 3.6 Mechanisms

282 The results presented above indicate that the SOM patterns explain nearly 40% of the trend in

283 wintertime surface air temperature anomalies and majority of the contributions (35 out of 40%) come

284 from the two pairs of the nodes (nodes 1, 9, and 4, 6). The analyses hereafter will focus on these four

285 nodes. Below we assess the atmospheric and oceanic conditions associated with the occurrences of the

286 four nodes via regression analysis. Specifically, the anomalous seasonal SST and atmospheric

287 circulation variables are regressed onto the normalized time series of the number of days when each of

288 the four nodes occurs (Figures 10, 11, and 12).

289 For node 1, the SST regression pattern in the Pacific Ocean shows significant positive anomalies

290 over the tropical western Pacific Ocean and central North Pacific Ocean (Figure 10). The positive SST

291 anomalies also occur over most of the North Atlantic. Negative SST anomalies occur over the central

292 tropical Pacific Ocean, though they are not significant at 95% confidence level. The SST regression

293 pattern is reversed for node 9. The direction of wave activity flux indicates the direction of group speed

294 of stationary planetary wave. Here we calculate the wave activity flux defined by Takaya and

295 Nakamura (2001), which considers the influence of mid-latitude zonal wind (Figure 12). For node 1,

296 the corresponding anomalous 500-hPa height regression (Figure 11) shows two Rossby wavetrains: one

297 is excited over the central Pacific Ocean and propagates northeastwards into North America and North

298 Atlantic Ocean, and the other, which displays astronger signal, originates from central North Atlantic

299 and propagates northeastwards to the Arctic Ocean and southeastwards to the Eurasian continent

300 (Figure 11 and 12). For node 9, the corresponding anomalous 500-hPa height and streamfunction show

301 an opposite pattern, but the wave activity flux is similar to that of node 1.

302 For node 4, the SST anomalies over the tropical Pacific Ocean appear to be in a La Niña state,

303 which shows stronger negative SST anomalies over the eastern tropical Pacific Ocean than those for

304 node 1 (Figure 10). The positive SST anomalies over the North Pacific shift more northwards relative

305 to that of node 1. The positive SST anomalies over the North Atlantic are weaker than those for node 1.

306 The corresponding wavetrain over the Pacific Ocean is stronger than that over the Atlantic Ocean

307 (Figure 11), which is also be observed in the pattern of wave activity and streamfunction (Figure 12).

308 The corresponding pattern for node 6 is nearly reversed, but there are some noticeable differences in

14

309   the amplitude of the wavetrain and SST anomalies. For example, the magnitude of the anomalous SST

310   and the 500-hPa height over the central North Pacific is larger for node 6 than that for node 4.

311   Besides the above-mentioned variables, similar regression analysis is also performed for the

312   anomalous 850-hPa wind field and anomalous downward longwave radiation (not shown). Their

313   regression patterns, which are similar to those in Figures 3 and 4, explain well the decadal variability of

314   the number of days for nodes 1, 4, 6, and 9. Together, these results in Figures 10-12 indicate that the

315   decadal variability of the occurrence frequency of the four nodes in recent decades is related to two

316   wavetrains induced by SST anomalies over the central North Pacific Ocean and the North Atlantic

317   Ocean (Figures 10 and 11). The aforementioned SST regression patterns over the Atlantic and Pacific

318   Oceans also show features of the AMO and PDO (Figure 10). Since both the AMO and PDO exhibited

319   a phase change in the late 1990s (Yu et al., 2017), the question is whether a similar change in the SOM

320   frequency also appear in the late 1990s. A comparison of the averaged frequency before and after 1998

321   shows a significant drop in frequency for nodes 6 and 9 and an increase in frequency for node 1 (not

322   shown). This result suggests that the change in the AMO and PDO indices may contribute to the change

323   in the frequencies of the warm Arctic-cold Eurasia continent pattern.

324   3.7 Interdecadal variability

325   The four-decade-long ERA-Interim reanalysis is not adequate for examining interdecadal to

326   multi-decadal variations represented by the PDO and AMO indices. Further analysis is performed using

327   the 20CR daily reanalysis data for the 1854-2014 period. Before applying the SOM technique to the

328   20CR data, we first remove the trend to eliminate the influence from the global warming. No low-pass

329   filter is applied before SOM analysis in order to test the stability of the SOM results for the different

330   periods. The spatial SOM patterns from the de-trended century-long 20CR data (Figure 13) are similar

to those for the 1979-2019 period (Figure 1). Nodes 1, 4, and 7 correspond to the positive phase of the

warm Arctic-cold Eurasia pattern and the negative phase can be observed in nodes 3, 6, and 9. The

magnitude in Figure 13 is smaller compared to the recent four decades in Figure 1. The occurrence

frequencies of the four nodes, 1, 4, 6, and 9 (Figure 14), are close to those for the recent four decades

(Figure 7). It indicates that the SOM method can obtain stably the main modes of wintertime surface

air temperature variability. For the recent four decades, the time series of the number of days also

displays a noticeable increasing (decreasing) trend for nodes 1 and 4 (6 and 9), suggesting that the

trend in the recent four decades is a reflection of an interdecadal variability of wintertime surface air

temperature.

　　　Next, we apply a 40-year low-pass filter to the time series of the occurrence frequencies for nodes

1, 4, 6 and 9 and the AMO and PDO indices and calculate correlations. There is a significant

correlation between the time series and the AMO index, with correlation coefficients of 0.36 for node 1,

0.27 for node 4, -0.37 for node 6, and -0.20 for node 9, all of which are at the 95% confidence level. No

significant correlations, however, are found between the filtered time series and the PDO index. If we

define a SST index to represent the variability of SST anomalies over the central North Pacific Ocean

(20 °N-40 °N, 150 °E-150 °W), the 40-year low-pass filtered central North Pacific Ocean SST index is

now significantly correlated with the filtered time series of occurrence frequencies for nodes 1 and 9

(0.55 for node 1 and -0.46 for node 9). The correlation results are consistent with the SST regression

map for the recent decades (Figure 10).

　　　To confirm the effect of SST anomalies on the warm Arctic -cold Eurasia pattern, we also perform

EOF analysis of wintertime detrended seasonal surface air temperature anomalies for the 1854-2014

period (Figure 15). The spatial patterns of the first and second EOF modes show the negative phase of

16

353   the warm Arctic-cold Eurasia pattern and the 40-year low-pass filtered time series is inversely

354   correlated with the 40-year low-pass filtered wintertime AMO index (-0.46, p<0.05 for mode 1 and

355   -0.44, p<0.05 for mode 2). The 40-year low-pass filtered time series of the two EOF modes have a

356   significant negative correlation with the 40-year low-pass filtered central North Pacific Ocean SST

357   index, with correlation coefficients of -0.19 and -0.26 (p<0.05). Only PC1 has a significant correlation

358   with the PDO index (0.38, p<0.05). Thus, the increase in the occurrence of the warm Arctic-cold

359   Eurasia pattern in the recent decades is a part of the interdecadal variability of the pattern, which is

360   influenced by the AMO index, the PDO index, and the central North Pacific SST.

361   **4 Conclusions and Discussions**

362   In this study, we examine the variability of wintertime surface air temperature in the Arctic and the

363   Eurasian continent (20°E-130°E) by applying the SOM method to daily temperature from the gridded

364   ERA-Interim dataset for the period 1979-2019 and from the 20CR reanalysis for the period 1854-2014

365   and the EOF method to seasonal temperature from the 20CR reanalysis for the period 1854-2014. The

366   spatial pattern in the surface temperature variations in the study region, as revealed by the nine SOM

367   nodes, is dominated by concurrent warming in the Arctic and cooling in Eurasia, and vice versa. The

368   nine SOM patterns explain nearly 40% of the trends in wintertime surface temperature and 88% of that

369   are accounted for by only four nodes. Two of the four nodes (nodes 1 and 4) represent the warm

370   Arctic-cold Eurasian pattern and the other two (nodes 6 and 9) depict the opposite cold Arctic-warm

371   Eurasia pattern. There is a clear shift in the frequency of the occurrence of these patterns near the

372   beginning of this century, with the warm Arctic – cold Eurasia pattern dominating since 2003, while the

373   opposite pattern prevailing from the 1980s through the 1990s. The warm Arctic-cold Eurasia pattern is

374   accompanied by an anomalous high pressure and anticyclonic circulation over the Eurasian continent.

375 The anomalous winds and the associated temperature and moisture advection interact with local

376 longwave radiative forcing and turbulent fluxes to produce positive (negative) temperature anomalies

377 in the Arctic (Eurasian continent). The circulation is reversed for the cold Arctic-warm Eurasia pattern.

378 The warm, moist air mass is advected to the Arctic by the anomalous atmospheric circulations and the

379 increased downward turbulent heat flux also explain sea ice melt in the Barents and Kara Seas. In other

380 words, the sea ice loss in the Barents and Kara Seas and the cooling of the Eurasian continent can both

381 be traced to anomalous atmospheric circulations.

382 Increasing occurrences of the warm Arctic-cold Eurasian continent pattern appear to relate to

383 rising SST over the central North Pacific and North Atlantic Oceans (positive AMO phase). The SST

384 anomalies trigger two Rossby wavetrains spanning from the North Pacific Ocean, North America, and

385 the North Atlantic Ocean to the Eurasian continent. The two wavetrains are strengthened through local

386 sea-atmosphere-ice interactions in mid-high latitudes, which influence the change in the occurrence

387 frequency of the warm Arctic-cold Eurasian continent pattern. Our results agree with those of previous

388 studies (Lee et al., 2011; Sato et al., 2014; Clark and Lee, 2019). But previous studies only focus on the

389 effects of SST anomalies over either North Pacific or North Atlantic Oceans. We also note that the two

390 wavetrains excited by SST anomalies over different oceans differ in amplitudes, leading to somewhat

391 different warm Arctic-cold Eurasia patterns.

392 Using century-long data, we show that the warm Arctic-cold Eurasia pattern is an intrinsic climate

393 mode, which has been stable since 1854. The recent increasing trend in its occurrence is a reflection of

394 an interdecadal variability of the pattern resulting from the interdecadal variability of SST anomalies

395 over the central Pacific Ocean and over the Atlantic Ocean represented by the AMO index. Sung et al.

396 (2018) investigated interdecadal variability of the warm Arctic and cold Eurasia pattern and considered

397 the variability of the SST over the North Atlantic as its origin. Our results suggest that the variability of

398 the SST over the North Pacific also plays an important role. However, internal atmospheric variability

399 remains another potential source. The Rossby wavetrains also lead to deepening of a trough in East

400 Asia and generate an anomalous low pressure and cold temperature in northern China (Figure 10),

401 which further suggests that a warmer Arctic, especially warmer Barents and Kara Seas is not the driver

402 for the increasing occurrence of cold spells in East Asia, as suggested in previous studies (Kim et al.,

403 2014; Mori et al., 2014; Kug et al., 2015; Overland et al., 2015).

404   Our results suggest that the increasing trend in warm Arctic-cold Eurasia pattern may be related to

405 the anomalous SST over the central North Pacific and the North Atlantic Oceans. But we cannot rule

406 out the influence of the Arctic sea ice loss on the trend. The Arctic sea ice loss results from both Arctic

407 warming due to anthropogenic increasing of greenhouse gas concentrations and natural variability of

408 climate system such as SST anomalies. This study considers natural variability or internal driver of

409 climate system. The Arctic warming caused external forcing related to increasing greenhouse gas

410 emissions can produce an anomalous anticyclone over the Barents and Kara Seas, leading to the warm

411 Arctic-cold continents pattern.

412   Although the ERA-Interim reanalysis is overall superior in describing the Arctic atmospheric

413 environment to other similar global reanalysis products, it contains warm and moist biases in the

414 surface layer (Jakobson et al., 2012; Chaudhuri et al., 2014; Simmons and Poli, 2015; Wang et al.,

415 2019). However, we believe these biases, as well as the relatively coarse resolution, should have

416 minimum impact in the results from the current analyses.   Further, although the current analyses were

417 performed on a predetermined SOM grid with 3x3 nodes, an increase in the number of SOM nodes

418 didn't change the conclusions.

419   Our results help broaden the current understanding of the formation mechanisms for the warm

420   Arctic-cold Eurasia pattern. The SST anomalies over Northern Hemisphere oceans may offer a

421   potential for predicting its occurrence. The statistical relationship between SST anomalies and the

422   occurrences of the warm Arctic-cold continents pattern may help improve the predictability of

423   wintertime surface air temperature over Eurasian continent on interdecadal time scales.

424   **Data Availability**

425   All data used in the current analyses are publicly available. The monthly sea ice concentration data are

426   available from the National Snow and Ice Data Center (NSIDC) (http://nsidc.org/data/NSIDC-0051), the

427   ERA-Interim reanalysis data are available from the European Center for Mid-Range Weather

428   Forecasting (https://www.ecmwf.int/en/forecasts/datasets/reanalysis-datasets/era-interim) and the sea

429   surface temperature data are available from the Hadley Centre for Climate Prediction and Research

430   (ftp://ftp.cdc.noaa.gov/Datasets/noaa.oisst.v2.highres/). The long-term SST data are derived from

431   from   the   Twentieth   Century   Reanalysis   project,   version   2c   (20CR)

432   (https://climatedataguide.ucar.edu/climate-data/noaa-20th-century-reanalysis-version-2-and-2c).

433   **Competing interests**

434   The authors declare that they have no conflict of interest.

435   **Author Contributions**

436   L. Yu designed the study, with input from S. Zhong, and carried out the analyses. L. Yu and S. Zhong

437   prepared the manuscript. C. Sui plotted a part of Figures. B. Sun revised the manuscript.

442

443

444   **References**

445   Barnes, E. A. and Screen, J. A.: The impact of Arctic warming on the midlatitude jet-stream: Can it?

446   Has it? Will it?, WIRES Clim. Change, 6, 277-286, doi:10.1002/wcc.337, 2015.

447   Blackport, R., Screen J. A., Wiel K. van der, and Bintanja, R.: Minimal influence of reducedArctic sea

448   ice on coincident cold winters in mid-latitudes, Nature Climate Change, 9,

449   doi:10.1038/s41558-019-0551-4, 2019, 2019.

450   Chaudhuri, A. H., Ponte, R. M., and Nguyen, A. T.: A Comparison of atmospheric reanalysis products

451   for the Arctic Ocean and implications for uncertainties in air-sea fluxes, J. Climate, 27,

452   5411-5421, doi:10.1175/JCLI-D-13-00424.1, 2014.

453   Chen, L., Francis J. and Hanna E.: The "Warm-Arctic/Cold continents" pattern during 1901-2010, Int. J.

454   Climatol., 38, 5245-5254, doi:10.1002/joc.5725, 2018.

455   Clark, J. P. and Lee, S.: The role of the tropically excited Arctic Warming Mechanism on the warm

456   Arctic cold continent surface air temperature trend pattern, Geophys. Res. Lett., 46, 8490-8499,

457   doi:10.1029/2019GL082714, 2019

458   Cohen, J., Screen, J. A., Furtado, J. C., Barlow, M., Whittleston, D., Coumou, D., Francis, J., Dethloff,

459   K., Entekhabi, D., Overland, J., and Jones, J.: Recent Arctic amplification and extreme

460   mid-latitude weather, Nat. Geosci., 7, 627-637, doi:10.1038/ngeo2234, 2014.

461   Cohen, J., Pfeiffer, K., and Francis, J. A.: Warm Arctic episodes linked with increased frequency of

462   extreme winter weather in the United States, Nat. Commun., 9, 869,

463   doi:10.1038/s41467-018-02992-9, 2018.

464   Compo, G. P., Whitaker, J. S., Sardeshmukh, P. D., Matsui, N., Allan, R., Yin, X., Jr, G. B. E., Vose, R.

465   S., Rutledge, G. K., Bessemoulin, P., Brönnimann, S., Brunet, M., Crouthamel, R. I., Grant, A.

466   N., Groisman, P. Y., Jones, P. D., Kruk, M. C., Kruger, A. C., Marshall, G. J., Maugeri, M., Mok,

467   H. Y., Nordli, Ø., Ross, T. F., Trigo, R. M., Wang, X., Woodruff, S. D., and Worley S. J.: The

468   Twentieth Century Reanalysis Project, Quart, J. Roy. Meteor. Soc., 137, 1-28,

469   doi:10.1002/qj.776, 2011.

470   Dee, D. P., Uppala, S. M., Simmons, A. J., Berrisford, P., Poli, P., Kobayashi, S., Andrac, U.,

471   Balmaseda, M. A., Balsamo, G., Bauer, P., Bechtold, P., Beljaars, A. C. M., van de Berg, L.,

472   Bidlot, J., Bormann, N., Delsol, C., Dragani, R., Fuentes, M., Geer, A. J., Haimberger, L., Healy,

473   S. B., Hersbach, H., Hólm, E. V., Isaksen, L., Kållberg, P., Köhler, Matricardi, M., McNally, A.

474   P., Monge-Sanz, B. M., Morcrette, J.-J., Park, B.-K., Peubey, C., de Rosnay, P., Tavolato, C.,

475   Thépaut, J.-N., and Vitart, F.: The ERA-Interim reanalysis: configuration and performance of the

476   data assimilation system, Q. J. R. Meteorol. Soc., 137, 553-597, doi:10.1002/qj.828, 2011.

477   Enfield, D. B., Mestas-Nunez, A. M., and Trimble, P. J.: The Atlantic multidecadal oscillation and it's

478   relation to rainfall and river flows in the continental U.S., Geophy. Res. Lett., 28, 2077-2080,

479   2001.

480   Fyfe, J. C.: Midlatitudes unaffected by sea ice loss, Nature Climate Change, 9,

481   doi:10.1038/s41558-019-0560-3, 2019 .

482   Gibson, P. B., Perkins-Kirkpatrick, S. E., Uotila, P., Pepler, A. S., and Alexander, L. V.: On the use of

483   self-organizing maps for studying climate extremes, J. Geophys. Res. Atmos., 122, 3891–3903,

484   doi:10.1002/2016JD026256, 2017.

485   Hoskins, B. and Woollings, T.: Pesistent extratropical regims and climate extremes, Curr. Clim. Change

486   Rep., 1, 115-124, doi:10.1007/s40641-015-0020-8, 2015

487   Horton, D. E., Johnson, N. C., Singh, D., Swain, D. L., Rajaratnam, B., and Diffenbaugh, N. S.:

488   Contribution of changes in atmospheric circulation patterns to extreme trends, Nature,

489   522,465-469, doi:10.1038/nature14550, 2015.

490   Inoue, J., Hori, M. E., and Takaya, K.: The role of Barents Sea ice in the wintertime cyclone track and

491   emergence of a warm-Arctic-Siberian anomaly, J. Clim., 25, 2561-2568,

492   doi:10.1175/JCLI-D-11-00449.1, 2012.

493   Jakobson, E., Vihma, T., Palo, T., Jakobson, L., Keernik, H., and Jaagus, J.: Validation of atmospheric

494   reanalyses over the central Arctic Ocean, Geophys. Res. Lett., 39, L10802,

495   doi:10.1029/2012GL051591, 2012.

496   Johnson, N. C. and Feldstein, S. B.: The continuum of North Pacific sea level pressure patterns:

497   Intraseasonal, interannual, and interdecadal variability, J. Clim., 23,

498   851-867, doi:10.1175/2009JCLI3099.1, 2010.

499   Jakobson, E., Vihma, T., Palo, T., Jakobson, L., Keernik, H., Jaagus, J.: Validation of atmospheric

500   reanalyses over the central Arctic Ocean, Geophys. Res. Lett., 39, 2012.

501   Kalnay, E., Kanamitsu, M., Kistler, R., Collins, W. G., Deaven, D., Gandin, L., Iredell, M., Saha, S.,

502   White, G., Woollen J.: The NCEP/NCAR 40-year reanalysis project, Bull. Amer. Meteor. Soc.,

503   77, 437-471,doi:10.1175/1520-0477(1996)077<0437:TNYRP>2.0.CO;2, 1996.

504   Kim, B.-M., Son, S.-W., Min, S.-K., Jeong, J.-H., Kim, S.-J., Zhang, X., Shim, T., and Yoon, J.-H.:

505   Weakening of the stratospheric polar vortex by Arctic sea-ice loss, Nature Commun., 5, 4646,

506   doi:10.1038/ncomms5646, 2014.

507   Kohonen, T.,: Self-Organizing Maps. 3rd ed. Springer, 501 pp, 2001.

508   Kug, J.-S., Jeong, J.-H., Jang, Y.-S., Kim, B.-M., Folland, C. K., Min, S.-K., and Son, S.-W.: Two

509   distinct infleunces of Arctic warming on cold winters over North America and East Asia, Nat.

510   Geosci., 8, 759-762, doi:10.1038/ngeo2517, 2015.

511 Lee, S., Gong, T., Johnson, N., Feldstein, S. B., and Polland, D.: On the possible link between tropical

512   convection and theNorthern Hemisphere Arctic surface air temperature change between 1958

513   and 2001, J. Clim., 24, 4350-4367,doi:10.1175/2011JCLI4003.1, 2011.

514 Lee, S. and Feldstein, S. B.: Detecting ozone- and greenhouse gas–driven wind trends with

515   observational data, Science, 339, 563–567, doi:10.1126/science.1225154, 2013.

516 Loikith, P. C. and Broccoli, A. J.: Comparison between observed and model-simulated atmospheric

517   circulation patterns associated with extreme temperature days over North America using CMIP5

518   historical simulations, J. Clim., 28, 2063-2079, doi:10.1175/JCLI-D-13-00544.1, 2015.

519 Luo, D., Xiao, Y., Yao, Y., Dai, A., Simmonds, I., and Franzke, C. L. E.: Impact of Ural blocking on

520   winter warm Arctic-cold Eurasian anomalies. Part I: Blocking-induced amplification, J. Clim.,

521   29, 3925-3947, doi:10.1175/JCLI-D-15-0611.1, 2016.

522 Mantua, N. J., Hare, S. R., Zhang, Y., Wallace, J. M., and Francis, R. C.: A Pacific interdecadal climate

523   oscillation with impacts on salmon production, Bull. Amer. Meteor. Soc., 78, 1069–1079, 1997.

524 Matsumura, S. and Kosaka, Y.: Arctic-Eurasian climate linkage induced by tropical ocean variability,

525   Nature Communications, 10, 3441, doi:10.1038/s41467-019-11359-7, 2019.

526 Mori, M., Watanabe, M., Shiogama, H., Inoue, J., and Kimoto, M.: Robust Arctic sea-ice influence on

527   the frequent Eurasian cold winters in past decades, Nat. Geosci., 7, 869-873,

528   doi:10.1038/ngeo2277, 2014.

529 Mori, M., Kosaka, Y., Watanabe, M., Nakamura, H., and Kimoto, M.: A reconciled estimate of the

530   influence of Arctic sea-ice loss on recent Eurasian cooling, Nat. Clim. Change, 9, 123-129,

531   doi:10.1038/s41558-018-0379-3, 2019.

532 McCusker, K. E., Fyfe, J. C., and Sigmond, M.: Twenty-five winters of unexpected Eurasian cooling

533   unlikely due to Arctic sea-ice loss, Nat. Geosci., 9, 838-842, doi:10.1038/ngeo2820, 2016.

534 Overland, J. E., Wood, K. R., and Wang, M.: Warm Arctic-cold continents: climate impacts of the

535   newly open Arctic sea, Polar Res., 30, 15787, doi:10.3402/polar.v30i0.15787, 2011.

536 Overland, J. E., Francis, J., Hall, R., Hanna, E., Kim, S.-J., and Vihma, T.: The melting Arctic and

537   Midlatitude weather patterns: Are they connected?, J. Clim., 28, 7917-7932,

538   doi:10.1175/JCLI-D-14-00822.1, 2015.

539 Palmer, T. N.: A nonlinear dynamical perspective on climate prediction, J. Clim., 12, 575-591, 1999.

540   doi:10.1175/1520-0442(1999)012<0575:ANDPOC>2.0.CO;2

541 Peings, Y.: Ural blocking as a driver of early-winter stratospheric warmings, Geophys. Res. Lett., 46,

542   5460-5468, doi:10.1029/2019GL082097, 2019.

543 Reusch, D. B., Alley, R. B., and Hewitson, B. C.: Relative performance of self-organizing maps and

544   principal component analysis in pattern extraction from synthetic climatological data, Polar

545   Geogr., 29, 188–212, doi:10.1080/789610199, 2005.

546 Reynolds, R. W., Smith, T. M., Liu, C., Chelton, D. B., Casey, K. S., Schlax, M. G.: Daily

547   High-Resolution-Blended Analyses for Sea Surface Temperature, J. Climate, 20, 5473-5496,

548   doi:10.1175/2007JCLI1824.1, 2007.

549 Sammon, J. W.: A non-linear mapping for data structure analysis, IEEE Trans. Computers, C-18,

550   401–409 , 1969.

551 Sato, K., Inoue, J., and Watanabe, M.: Influence of the Gulf Stream on the Barents Sea ice retreat and

552   Eurasian coldness during early winter, Environ. Res. Lett., 9, 084009,

553   doi:10.1088/1748-9326/9/8/084009, 2014.

554 Schudeboom, A., McDonald, A. J., Morgenstern, O., Harvey, M., and Parsons, S.: Regional

555 regime-based evaluation of present-day GCM cloud simulations using self-organizing maps, J.

556 Geophys. Res. Atmos., 123, 4259–4272, doi:10.1002/2017JD028196, 2018.

557 Screen, J. A. and Simmonds, I.: The central role of diminishing sea ice in recent Arctic temperature

558 amplification, Nature, 464, 1334-1337, doi:10.1038/nature09051, 2010.

559 Screen, J. S. and Simmonds, I.: Erroneous Arctic temperature trends in the ERA-40 reanalysis: A closer

560 look, J. Clim., 24, 2620–2627, doi:10.1175/2010JCLI4054.1, 2011.

561 Sedlar, J., Tjernström, M., Mauritsen, T., Shupe, M. D., Brooks, I. M., PPersson, O., Birch, C. E., Leck,

562 C., Sirevaag, A., and Nicolaus, M. : A transitioning Arctic surface energy budget: The impacts of

563 solar zenith angle, surface albedo and cloud radiative forcing，Clim. Dyn., 37, 1643–1660,

564 doi:10.1007/s00382-010-0937-5, 2011.

565 Shepherd, T. G.: Effects of a warming Arctic, Science, 353, 989-990, doi:10.1126/science.aag2349,

566 2016.

567 Simmons, A., and Poli, P.: Arctic warming in ERA-Interim and other analyses, Q. J. R. Meteorol. Soc.,

568 141, 1147-1162, doi:10.1002/qj.2422, 2015.

569 Skific, N., Francis, J. A., and Cassano, J. J.: Attribution of projected changes in atmospheric moisture

570 transport in the Arctic: A self-organizing map perspective, J. Clim., 22, 4135-4153,

571 doi:10.1175/2009JCLI2645.1, 2009.

572 Sorokina, S. A., Li, C., Wettstein, J. J., and Kvamstø, N. G.: Observed atmospheric coupling between

573 Barents sea ice and the warm-Arctic cold-Siberian anomaly pattern, J. Clim., 29, 495-511,

574 doi:10.1175/JCLI-D-15-0046.1, 2016.

575 Stroeve, J. C., , Holland, M. M., Meier, W., Scambos, T., and Serreze, M.: Arctic sea ice decline: faster

576 than forecast, Geophys. Res. Lett., 34, L09051, doi:10.1029/2007gl029703, 2007.

577 Stroeve, J. C.: Trends in Arctic sea ice extent from CMIP5, CMIP3 and observations, Geophys. Res.

578 lett., 39, L16502, doi:10.1029/2012GL052676 , 2012.

579 Sun, L., Perlwitz, J., and Hoerling, M.: What caused the recent "warm Arctic-Cold Continents" trend

580 pattern in winter temperature?, Geophys. Res. Lett., 43, 5345-5352,

581 doi:10.1002/2016GL069024, 2016.

582 Sung, M.-K., Kim, S.-H., Kim, B.-M., and Choi, Y.-S.: Interdecadal variability of the warm Arctic and

583 cold Eurasia pattern and its North Atlantic origin, J. Clim., 31, 5793-5810,

584 doi:10.1175/JCLI-D-17-0562.1, 2018.

585 Tang, Q., Zhang, X., Yang, X., and Francis J. A.: Cold winter extremes in northern conditions linked to

586 Arctic sea ice loss, Environ. Res. Lett., 8, 014036, doi:1088/1748-9326/8/1/014036 ,2013.

587 Takaya K, and Nakamura, H.: A formulation of a phase-independent wave-activity flux for stationary

588 and migratory quasigeostrophic eddies on a zonally varying basic flow, J. Atmos. Sci., 58,

589 608-627, 2001.

590 Uppala, S., KÅllberg, P. W., Simmons, A. J., Andrae, U., Da Costa Bechtold, V., Florino, M., Gibson, J.

591 K., Haseler, J., Hernandez, A., Kelly, G. A., Li, X., Onogi, K., Saarinen, S., Sokka, N., Allan, R.

592 P., Andersson, E., Arpe, K., Balmaseda, M. A., Beljaars, A. C. M., Van De Berg, L., Bidlot, J.,

593 Bormann, N., Caires, S., Chevallier, F., Dethof, A., Dragosavac, M., Fisher, M., Fuentes, M.,

594 Hagemann, S., Hólm, E., Hoskins, B. J., Isaksen, L., Janssen, P. A. E. M., Jenne, R., Mcnally, A.

595 P., Mahfouf, J.-F., Morcrette, J.-J., Rayner, N. A., Saunders, R. W., Simon, P., Sterl, A.,

596 Trenberth, K. E., Untch, A., Vasiljevic, D., Viterbo, P., and Woollen, J.: The ERA-40 re-analysis,

597 Quarterly Journal of the Royal Meteorological Society, 131, 2961–3012, doi:10.1256/qj.04.176,

598   2005.

599   Walsh, J. E.: Intensified warming of the Arctic: Causes and impacts on middle Latitudes, Glob. Planet.

600   Change, 117, 52-63, doi:10.1016/j.gloplacha.2014.03.003 , 2014.

601   Vihma, T.: Effects of Arctic sea ice decline on weather and climate: A review, Surv. Geophys., 35,

602   1175-1214, doi:10.1007/s10712-014-9284-0 , 2014.

603   Vihma, T., Graversen, R., Chen, L., Handorf, D., Skific, N., Francis, J. A., Tyrrell, N., Hall, R., Hanna,

604   E., Uotila, P., Dethloff, K., Karpechko, A. Y., Björnsson, H., and Overland, J. E.: Effects of the

605   tropospheric large-scale circulation on European winter temperatures during the period of amplified

606   Arctic warming, Int. J. Climatol., doi:10.1002/joc.6225, 2019.

607   Wang, C., Graham, R. M., Wang, K., Gerland, S., Granskog, M. A.: Comparison of ERA5 and

608   ERA-Interim near-surface air temperature, snowfall and precipitation over Arctic sea ice: effects

609   on sea ice thermodynamics and evolution, The Cryosphere, 13, 1661-1679, 2019.

610   Yoo, C., Feldstein, S., and Lee, S.: The impact of the Madden–Julian oscillation trend on the Arctic

611   amplification of surface air temperature during the 1979–2008 boreal winter, Geophys. Res.

612   Lett., 38, L24804, doi:10.1029/2011GL049881, 2011.

613   Yu, L., Zhong, S., Winkler, J. A., Zhou, M., Lenschow, D. H., Li, B., Wang, X., and Yang, Q.: Possible

614   connections of the opposite trends in Arctic and Antarctic sea-ice cover, Scientific Reports, 7,

615   45804, doi:10.1038/srep45804, 2017.

616

617

618

619 Table 1. Spatial correlations (Corrs) between the daily winter (DJF) surface air

620 temperature and the corresponding SOM pattern for each day from 1979 to 2018.

	3×1	2×2	3×2	4×2	3×3	5×2	4×3	5×3	4×4
Corr	0.26	0.43	0.48	0.48	0.50	0.49	0.50	0.51	0.51

621

622

623

624

625

626

627
628
629
630
631
632
633
634
635
636
637
638
639
640
641
642
643
644
645
646
647
648
649
650

Table 2. Averaged anomalous NAO and AO indices for all occurrences of each SOM node. Asterisks indicate the above 95% confidence level.

	Node1	Node2	Node3	Node4	Node5	Node6	Node7	Node8	Node9
NAO	0.38*	0.22*	0.12*	0.05	-0.22*	-0.02	-0.07	-0.31*	-0.32*
AO	0.44*	0.38*	1.03*	-0.42	-0.62*	0.22*	-0.44*	-1.11*	-0.41*

692 Table 3. Trends in the frequency of occurrences for each SOM node (day yr^{-1}).
693 Asterisks indicate the above 95% confidence level.
694

	Node1	Node2	Node3	Node4	Node5	Node6	Node7	Node8	Node9
Trend	0.80*	0.10	-0.18	0.22*	-0.02	-0.39*	0.17	-0.17	-0.50*

695
696
697
698
699
700
701
702
703
704
705
706
707
708
709
710
711
712
713
714
715
716
717
718
719
720
721
722
723
724
725
726
727
728
729
730
731

Table 4. Frequencies of occurrence (%) of wintertime surface air temperature patterns in Figure 1 for all winters before 1998 and after 1998 for the period 1979-2019. Values with Asterisks are significantly different from climatology above the 95% confidence level.

| SOM patterns	Frequencies of occurrence		
	All winters	Winters before 1998	Winters after 1998
Node 1	17.1	7.4*	26.8
Node 2	4.4	3.3	5.4
Node 3	17.2	18.8	15.6
Node 4	8.6	5.4	11.7
Node 5	3.4	3.4	3.5
Node 6	10.2	15.2*	2.1*
Node 7	13.7	10.6	16.8
Node 8	10.1	12.1	8.0
Node 9	15.4	23.7*	7.1*

Figure Captions

Figure 1. Spatial patterns of SOM nodes for daily wintertime (December, January, and February) surface air temperature anomalies (℃) from ERA-Interim reanalysis over the 1979-2019 period. The number in brackets denotes the frequency of the occurrence for each node.
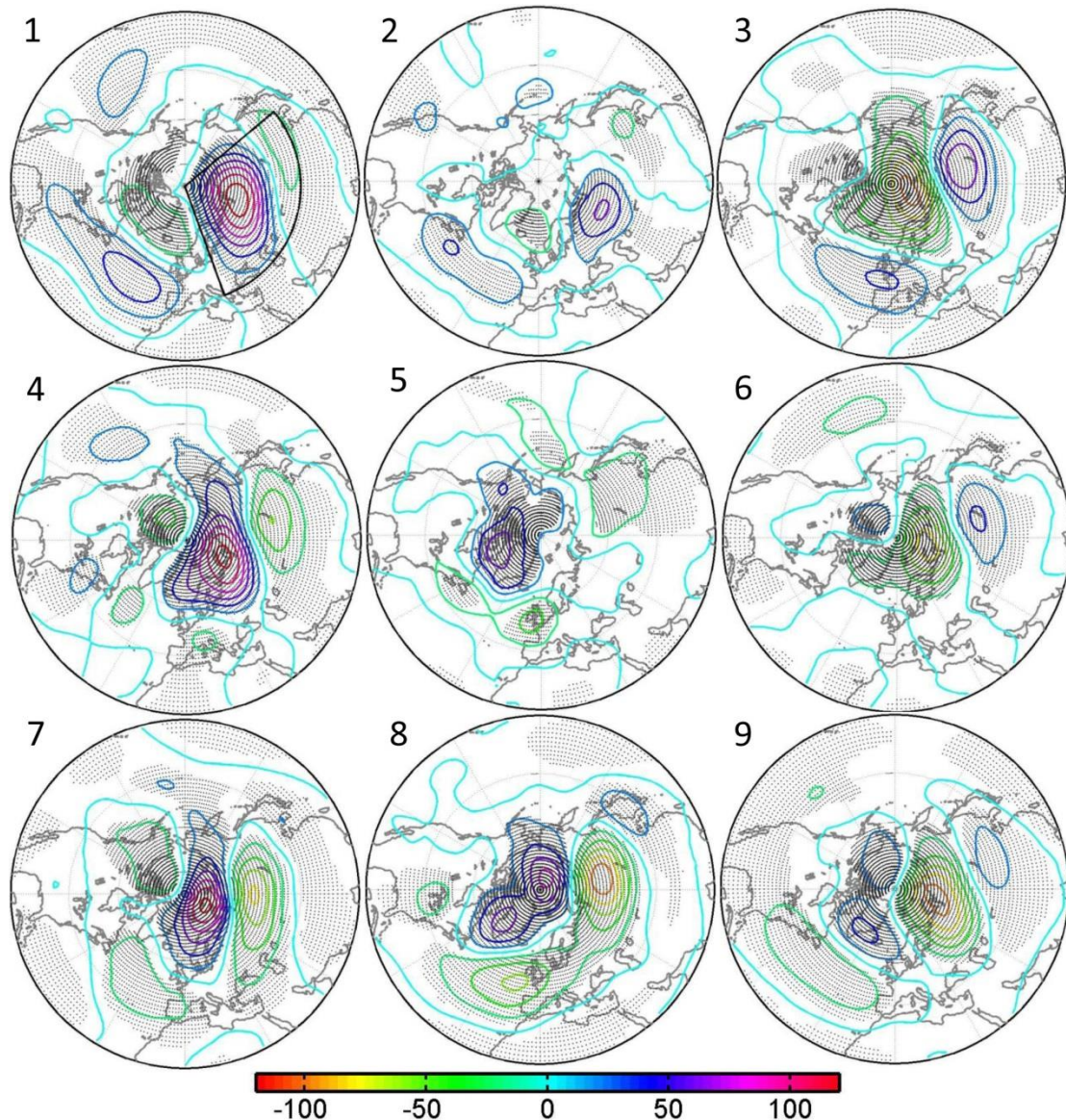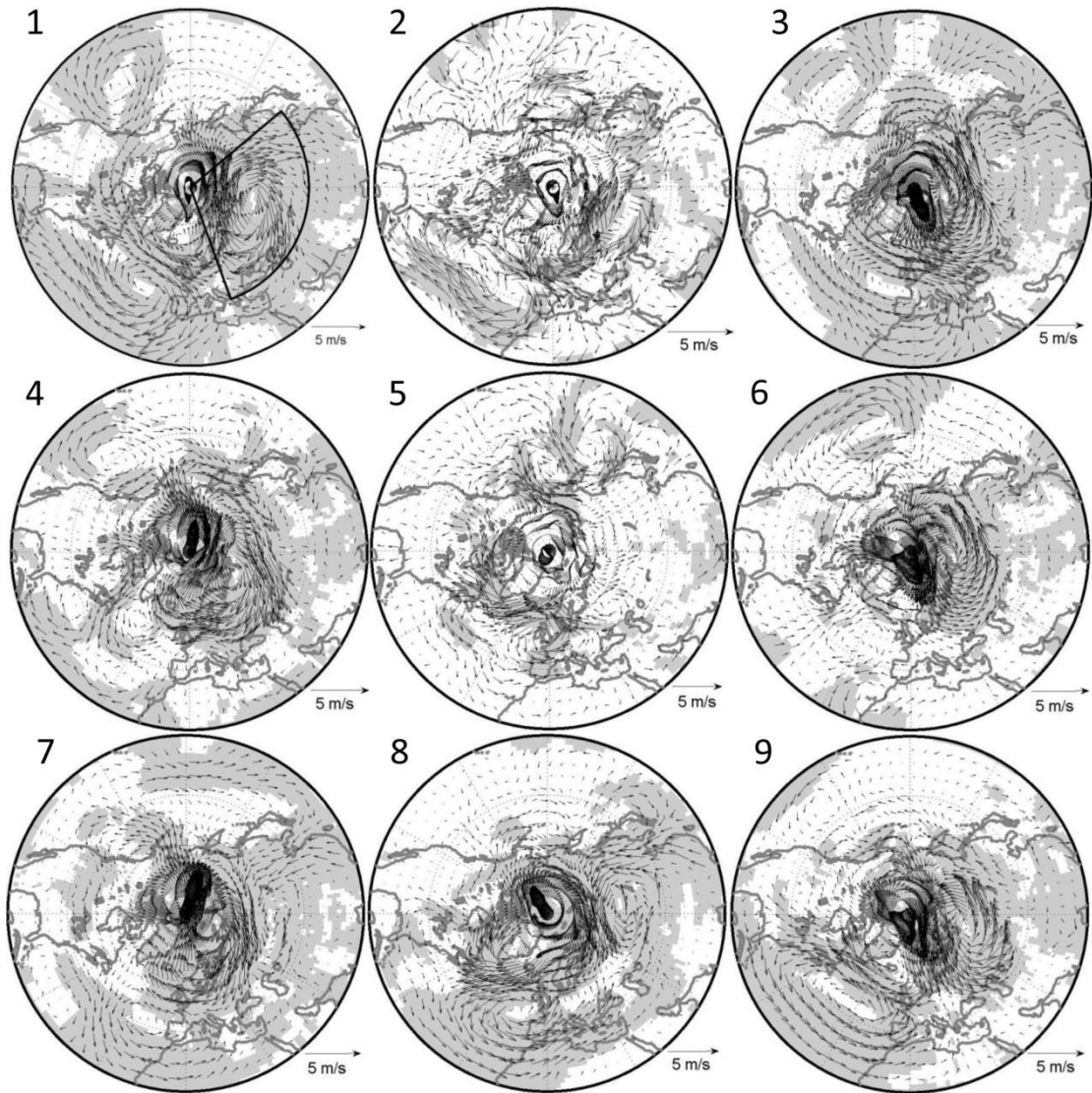
Figure 2. Corresponding 500-hPa geopotential height anomalies (gpm) from ERA-Interim reanalysis over the 1979-2019 period for each node in Figure 1. Dotted regions indicate the above 95% confidence level. The sub-domain in 1 shows the study region.

Figure 3. Corresponding anomalous 850-hPa wind field (m s^{-1}) from ERA-Interim reanalysis over the 1979-2019 period for each node in Figure 1. Shaded regions indicate the above 95% confidence level.

Figure 4. Corresponding anomalous daily accumulated downward longwave radiation (105 W m^{-2}) from ERA-Interim reanalysis over the 1979-2019 period for each node in Figure 1. Dotted regions indicate the above 95% confidence level.

Figure 5. Corresponding anomalous daily accumulated turbulent heat flux (sensible and latent heat) (10^5W m^{-2}) from ERA-Interim reanalysis over the 1979-2019 period for each node in Figure 1. Positive values denote heat flux from atmosphere to ocean and vice versa. Dotted regions indicate the above 95% confidence level.

Figure 6. Corresponding anomalous wintertime sea ice concentration from the NSIDC over the 1979-2019 period for each node in Figure 1. Dotted regions indicate the above 95% confidence level.

786   Figure 7. Time series of the number of days for occurrence of each SOM node in

787   Figure 1 over the 1979-2019 period. The red lines denote the trend in time series.

788   Figure 8. Total (top), SOM-explained (middle), and residual (bottom) trend in

789   wintertime (DJF) surface air temperature (^{o}C yr^{-1}) over the 1979-2019 period. Dots in

790   the top panel indicate above 95% confidence level.

791   Figure 9. Trends in surface air temperature explained by each SOM node (^{o}C yr^{-1})

792   over the 1979-2019 period. The percentage in the upper of each panel indicates the

793   fraction of the total trend represented by each node.

794   Figure 10. Anomalous SST (^{o}C) from the NOAA over the 1979-2019 period regressed

795   into the normalized time series of occurrence number for nodes 1, 4, 6, and 9.

796   Figure 11. Anomalous 500-hPa geopotential height (gpm) from ERA-Interim

797   reanalysis over the 1979-2019 period regressed into the normalized time series of

798   occurrence number for nodes 1, 4, 6, and 9.

799   Figure 12. The anomalous wave activity flux (vectors) (Takaya and Nakamura, 2001)

800   and stream function (colors, units: 10^{7} m^{2} s^{-1}) from ERA-Interim reanalysis over the

801   1979-2019 period regressed onto the normalized time series of occurrence number for

802   nodes 1, 4, 6, and 9.

803   Figure 13. Spatial patterns of SOM nodes for detrended daily wintertime (December,

804   January, and February) surface air temperature anomalies (^{o}C) from the 20CR

805   reanalysis for the 1851-2014 period. The number in brackets denotes the frequency of

806   the occurrence for each node.

807   Figure 14. Time series of the number of days for occurrence of each SOM node in

808   Figure 13 from the 20CR reanalysis for the 1851-2014 period. The thick red lines

809   denote the result in Figure 7 from the ERA-Interim reanalysis for the 1979-2019

810   period.

811   Figure 15. The (a) leading pattern and (b) its time series (PC1 and PC2) of EOF

812   analysis of wintertime surface air temperature anomalies from the 20CR reanalysis for

813   the 1851-2014 period. Prior to EOF analysis, surface sir temperature data are

814   detrended. A 40-yr low-pass filtered is applied to the time series of PC1, PC2, AMO,

815   PDO, and central North Pacific Ocean (CNPO) indices. The correlation coefficients

816   between PC1 and AMO, PDO and CNPO indices are -0.46 (p<0.0001), 0.38

817   (p<0.0001), and -0.19 (p=0.019); those between PC2 and and AMO, PDO and CNPO

818   indices are -0.44 (p<0.0001), 0.38 (p<0.0001), and -0.26 (p=0.0009).

819

820

821

822

823

824

825

826
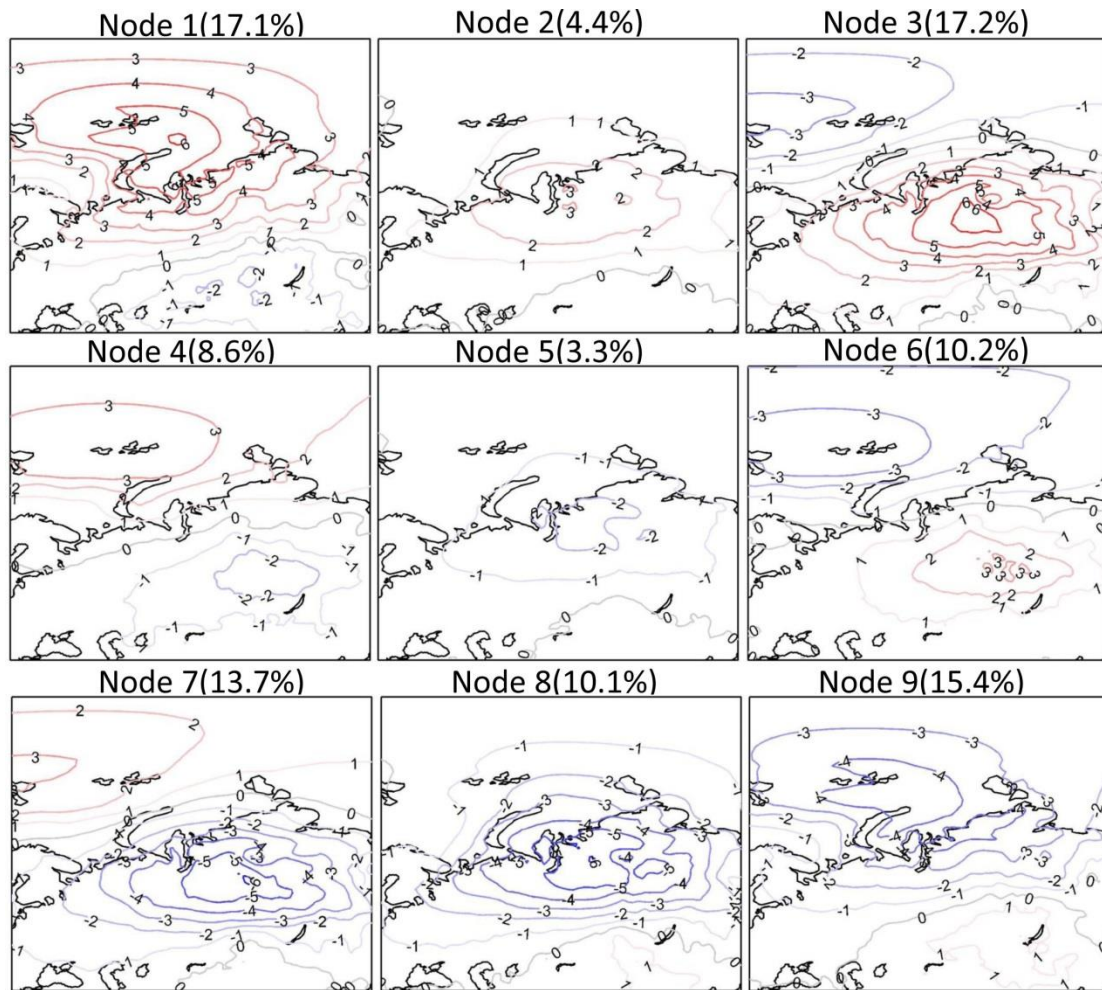
Figure 1. Spatial patterns of SOM nodes for daily wintertime (December, January, and February) surface air temperature anomalies (°C) from ERA-Interim reanalysis over the 1979-2019 period. The number in brackets denotes the frequency of the occurrence for each node.

Figure 2. Corresponding 500-hPa geopotential height anomalies (gpm) from ERA-Interim reanalysis over the 1979-2019 period for each node in Figure 1. Dotted regions indicate the above 95% confidence level. The sub-domain in 1 shows the study region.

Figure 3. Corresponding anomalous 850-hPa wind field from ERA-Interim reanalysis over the 1979-2019 period for each node in Figure 1. Shaded regions indicate the above 95% confidence level.

Figure 4. Corresponding anomalous daily accumulated downward longwave radiation (10^5 W m^{-2}) from ERA-Interim reanalysis over the 1979-2019 period for each node in Figure 1. Dotted regions indicate the above 95% confidence level.
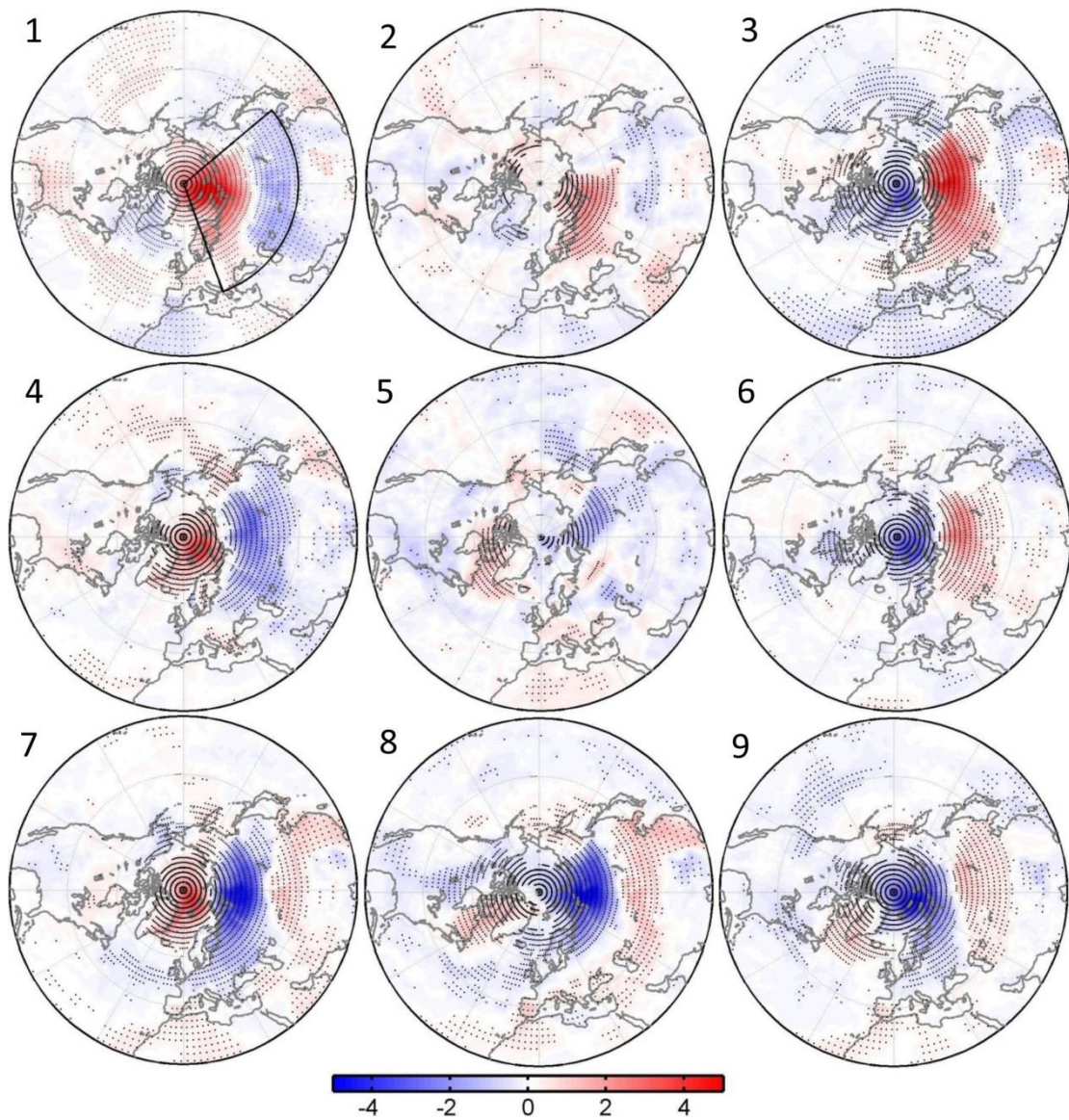
Figure 5. Corresponding anomalous daily accumulated turbulent heat flux (sensible and latent heat) (10^5W m^{-2}) from ERA-Interim reanalysis over the 1979-2019 period for each node in Figure 1. Positive values denote heat flux from atmosphere to ocean and vice versa. Dotted regions indicate the above 95% confidence level.
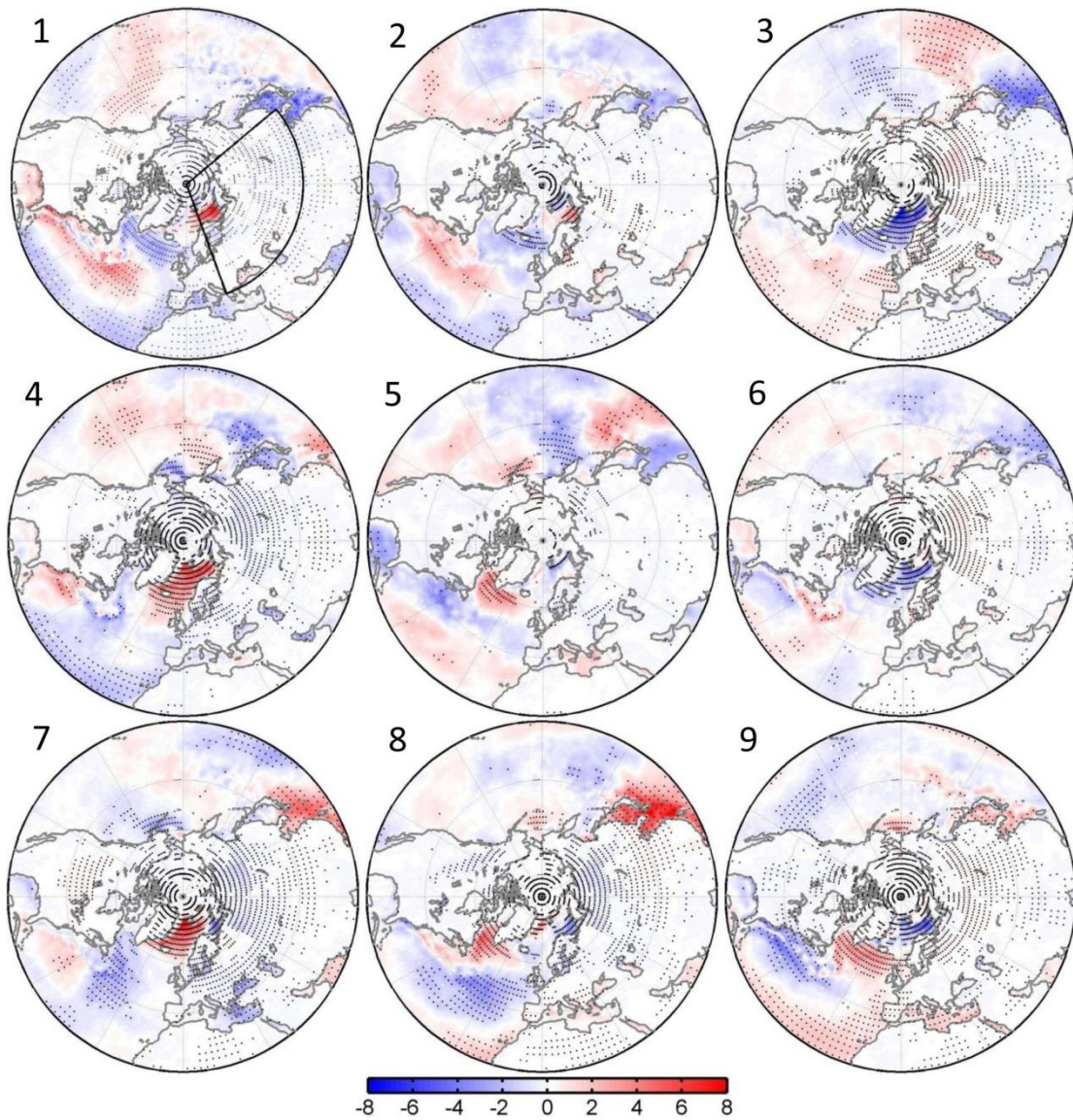
903
904
905
906
907
908

Figure 6. Corresponding anomalous wintertime sea ice concentration from the NSIDC over the 1979-2019 period for each node in Figure 1. Dotted regions indicate the above 95% confidence level.
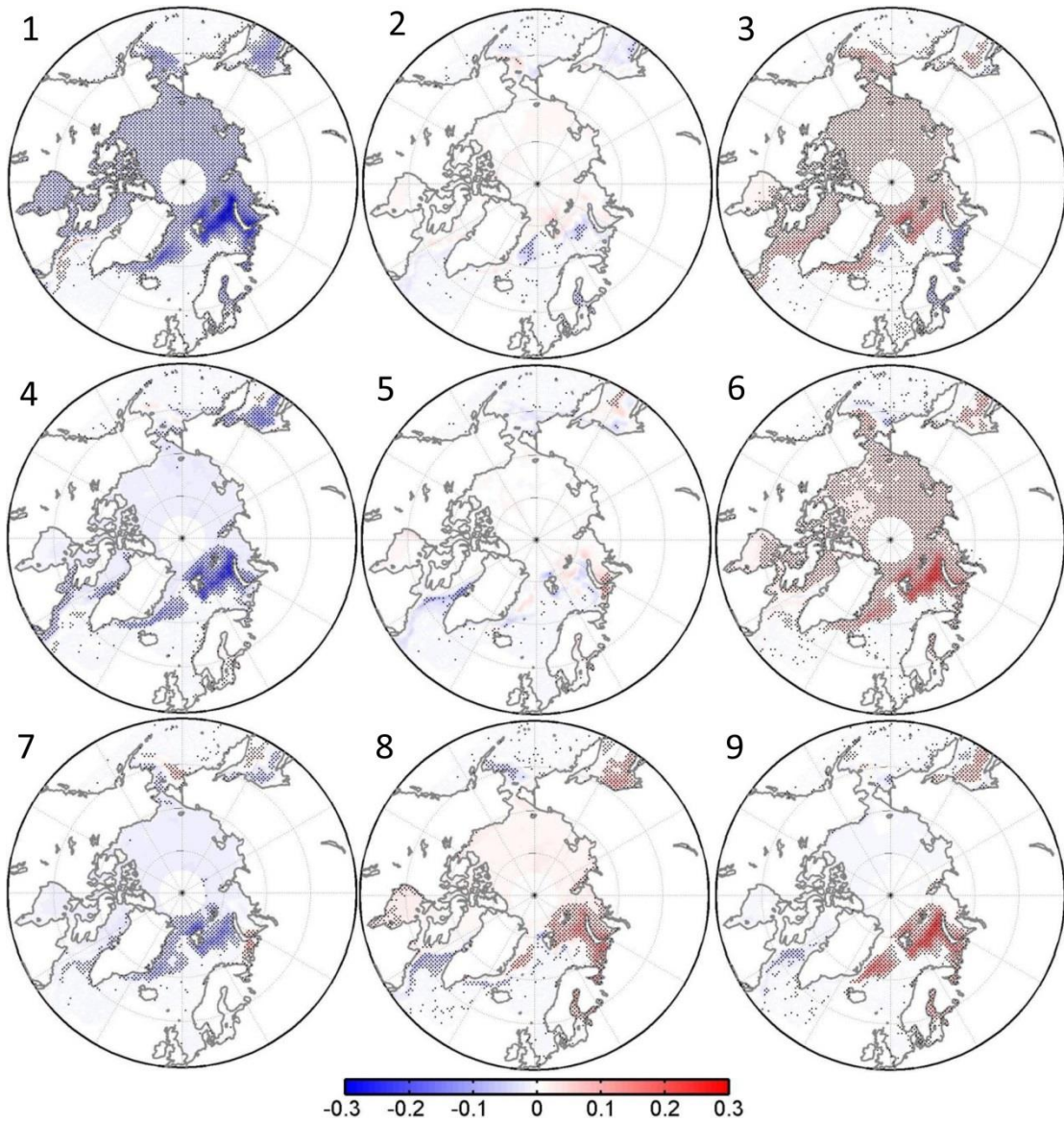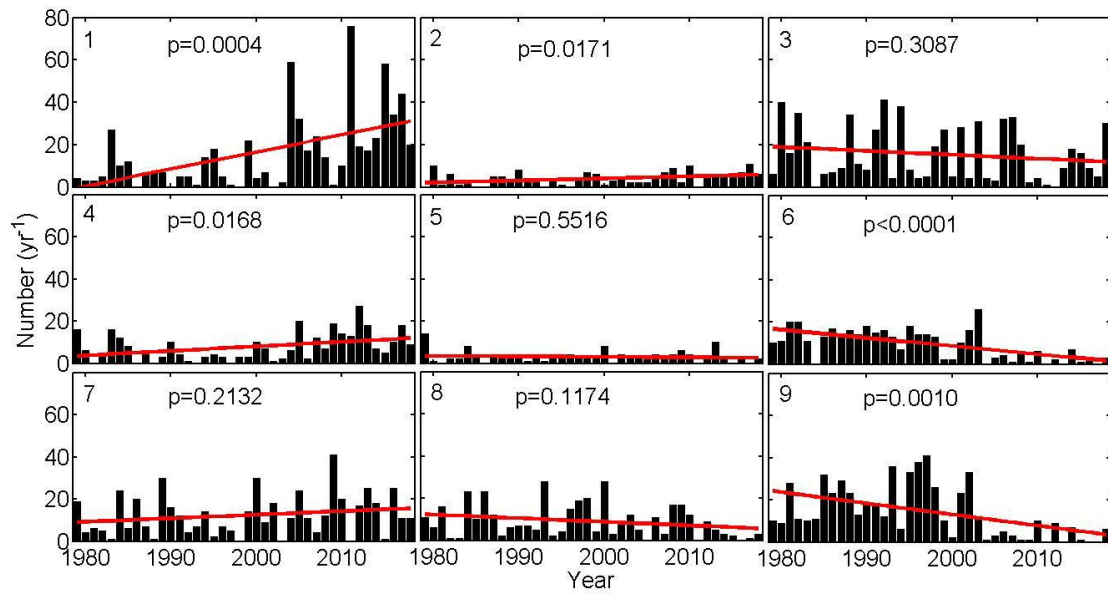
Figure 7. Time series of the number of days for occurrence of each SOM node in Figure 1 over the 1979-2019 period. The red lines denote the trend in time series.

929
930
931
932
933
934
935
936
937
938
939
940
941
942
943
944
945
946
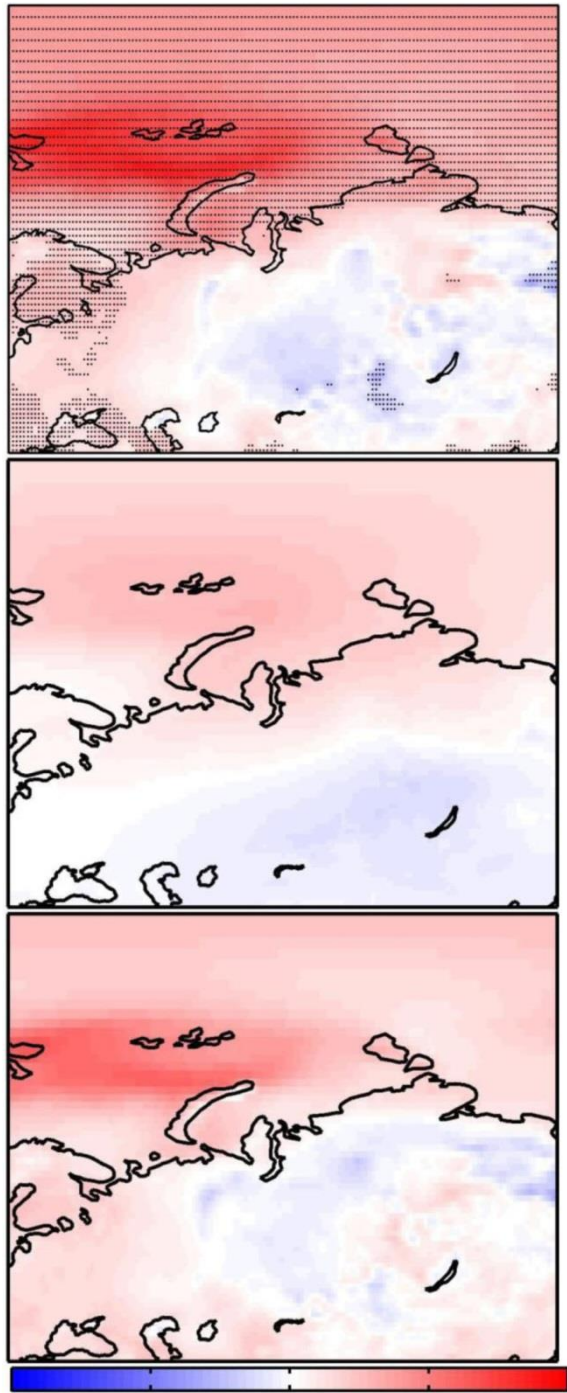
Figure 8. Total (top), SOM-explained (middle), and residual (bottom) trend in wintertime (DJF) surface air temperature (^{o}C yr^{-1}) over the 1979-2019 period. Dots in the top panel indicate above 95% confidence level.
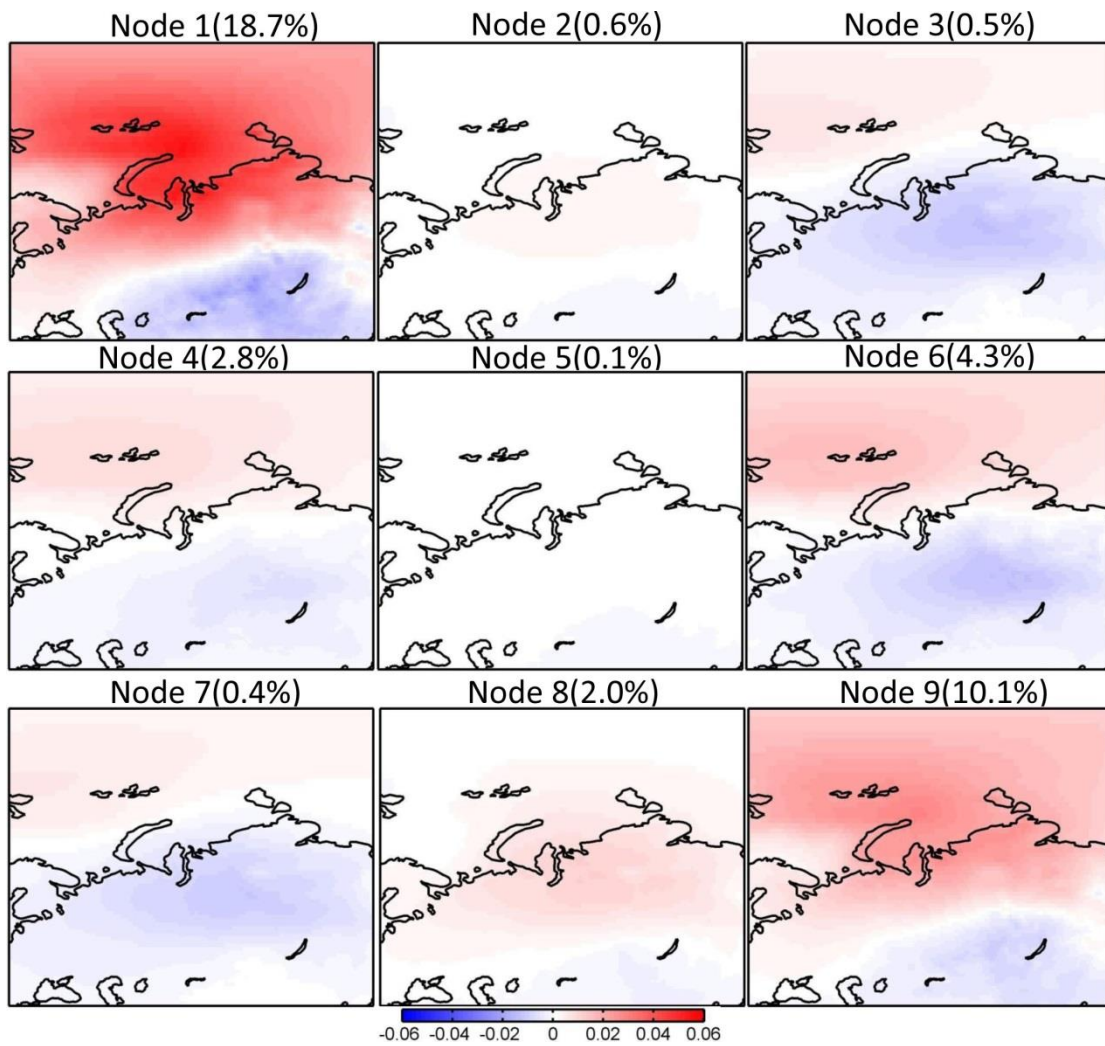
Figure 9. Trends in surface air temperature explained by each SOM node ($°C$ yr^{-1}) over the 1979-2019 period. The percentage in the upper of each panel indicates the fraction of the total trend represented by each node.
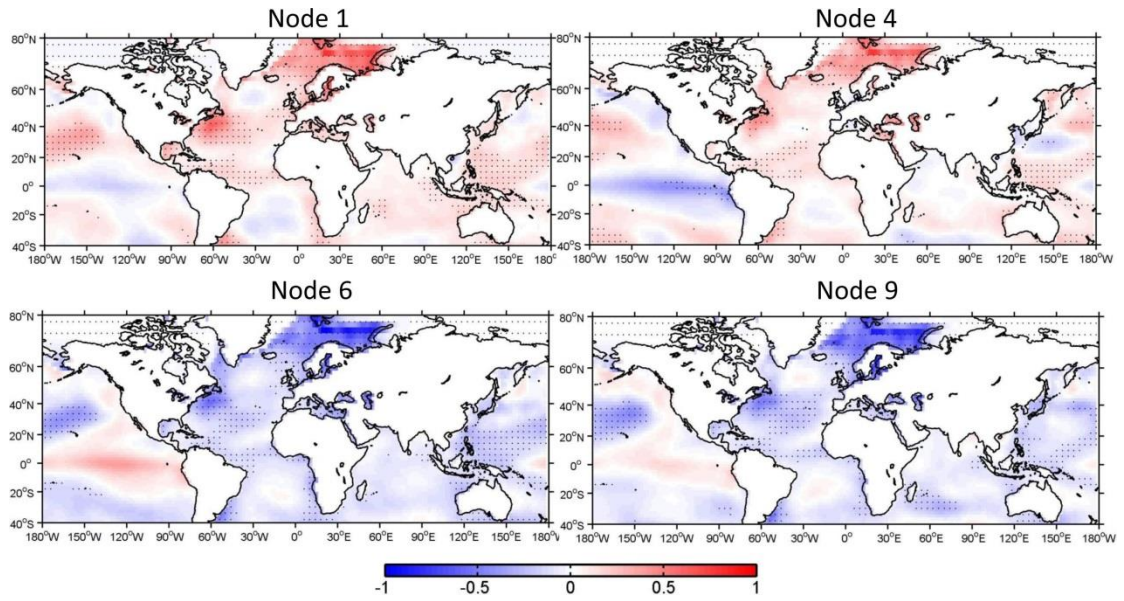
Figure 10. Anomalous SST (°C) from the NOAA over the 1979-2019 period regressed into the normalized time series of occurrence number for nodes 1, 4, 6, and 9.

974
975
976
977
978
979
980
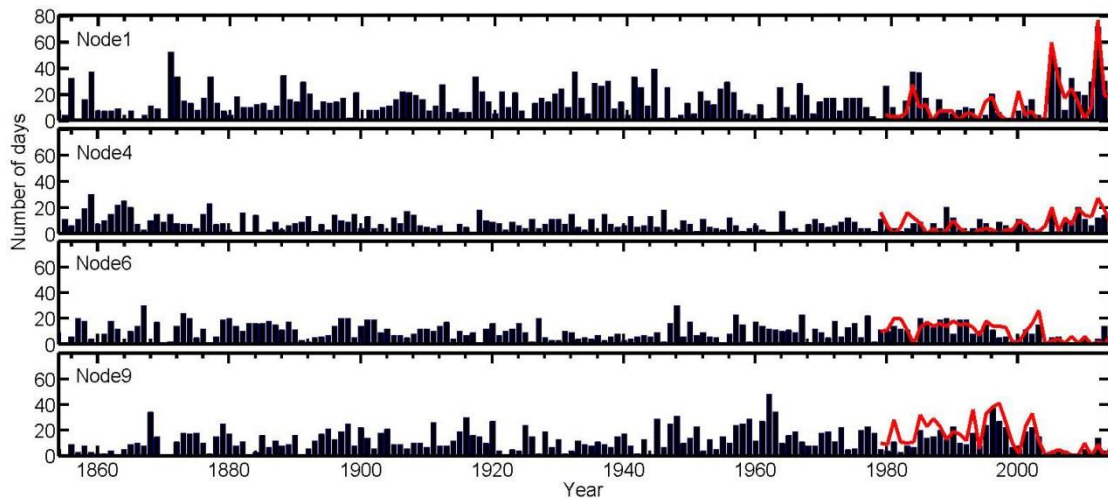981
982
983
984
985
986
987
988
989
990
991
992
993
994
995
996
997
998
999
1000
1001

Figure 11. Anomalous 500-hPa geopotential height (gpm) from ERA-Interim reanalysis over the
1979-2019 period regressed into the normalized time series of occurrence number for nodes 1, 4, 6,
and 9.
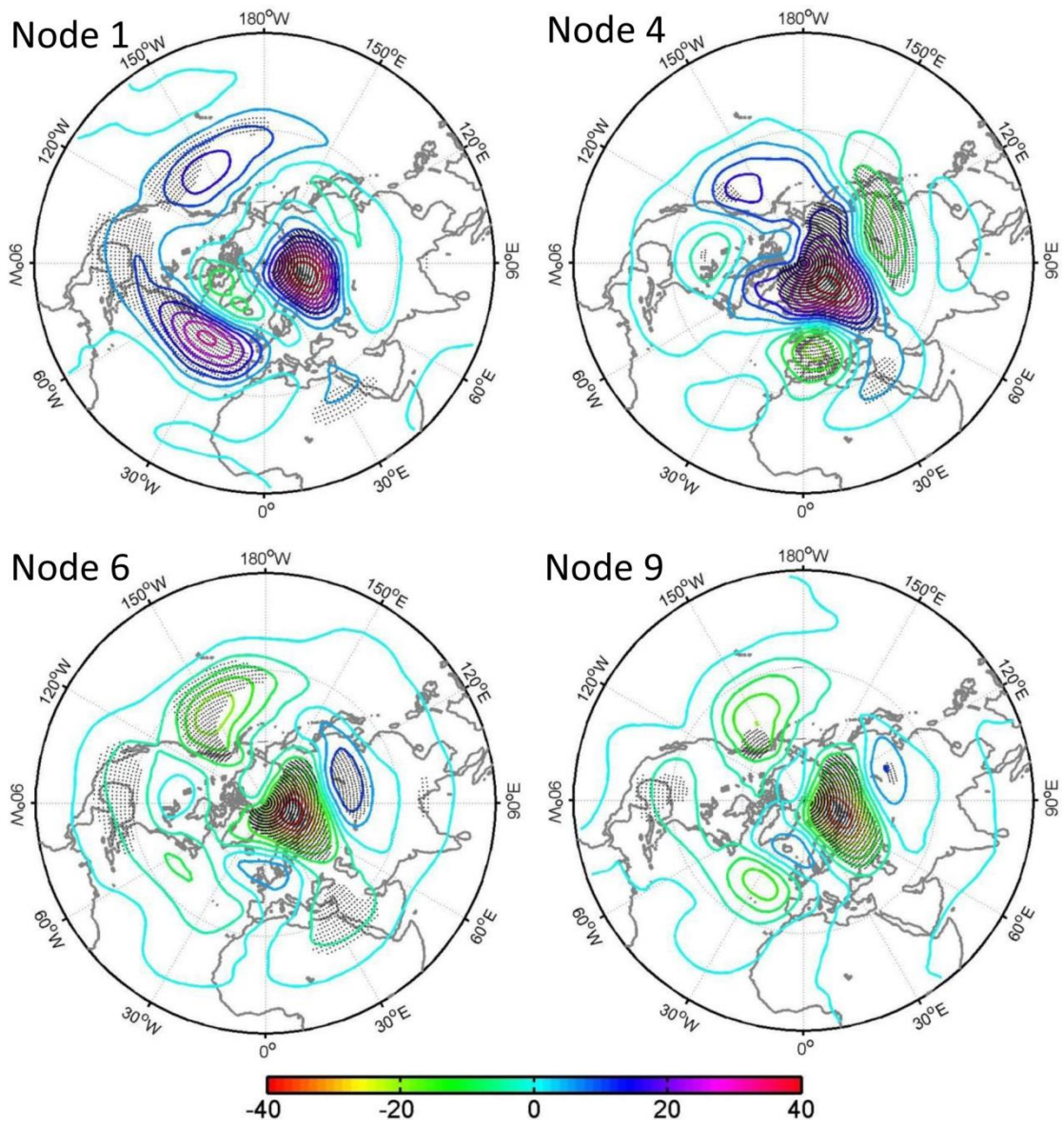
1009
1010
1011
1012
1013
1014
1015
1016
1017
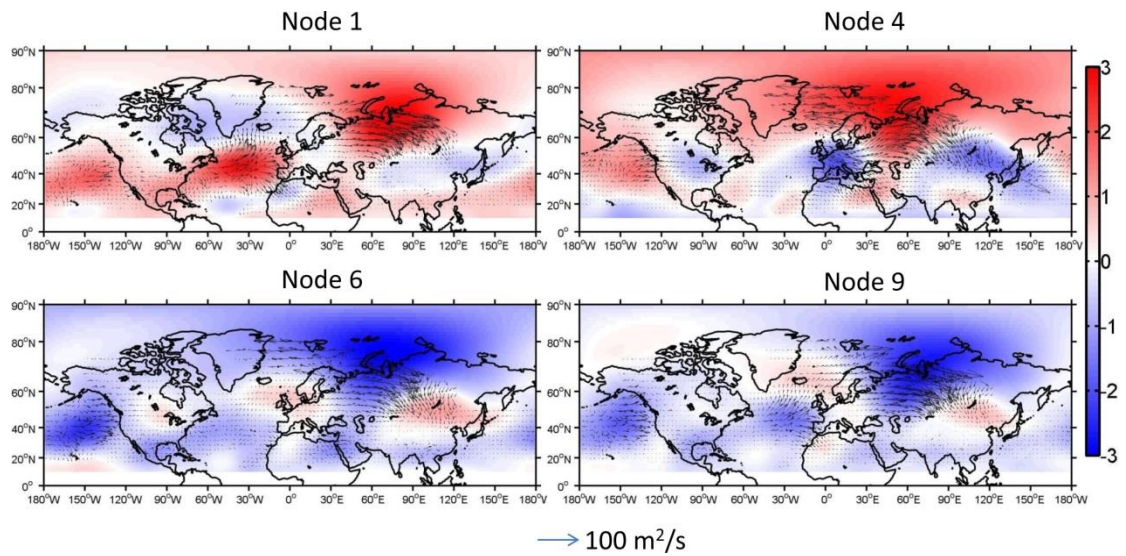
Figure 12. The anomalous wave activity flux (vectors) (Takaya and Nakamura, 2001) and stream function (colors, units: $10^7 \text{m}^2 \text{ s}^{-1}$) from ERA-Interim reanalysis over the 1979-2019 period regressed onto the normalized time series of occurrence number for nodes 1, 4, 6, and 9.

1022
1023
1024
1025
1026
1027
1028
1029
1030
1031
1032
1033
1034

Figure 13. Spatial patterns of SOM nodes for detrended daily wintertime (December, January, and February) surface air temperature anomalies (℃) from the 20CR reanalysis for the 1851-2014 period. The number in brackets denotes the frequency of the occurrence for each node.

Figure 14. Time series of the number of days for occurrence of each SOM node in Figure 13 from the 20CR reanalysis for the 1851-2014 period. The thick red lines denote the result in Figure 7 from the ERA-Interim reanalysis for the 1979-2019 period.

49
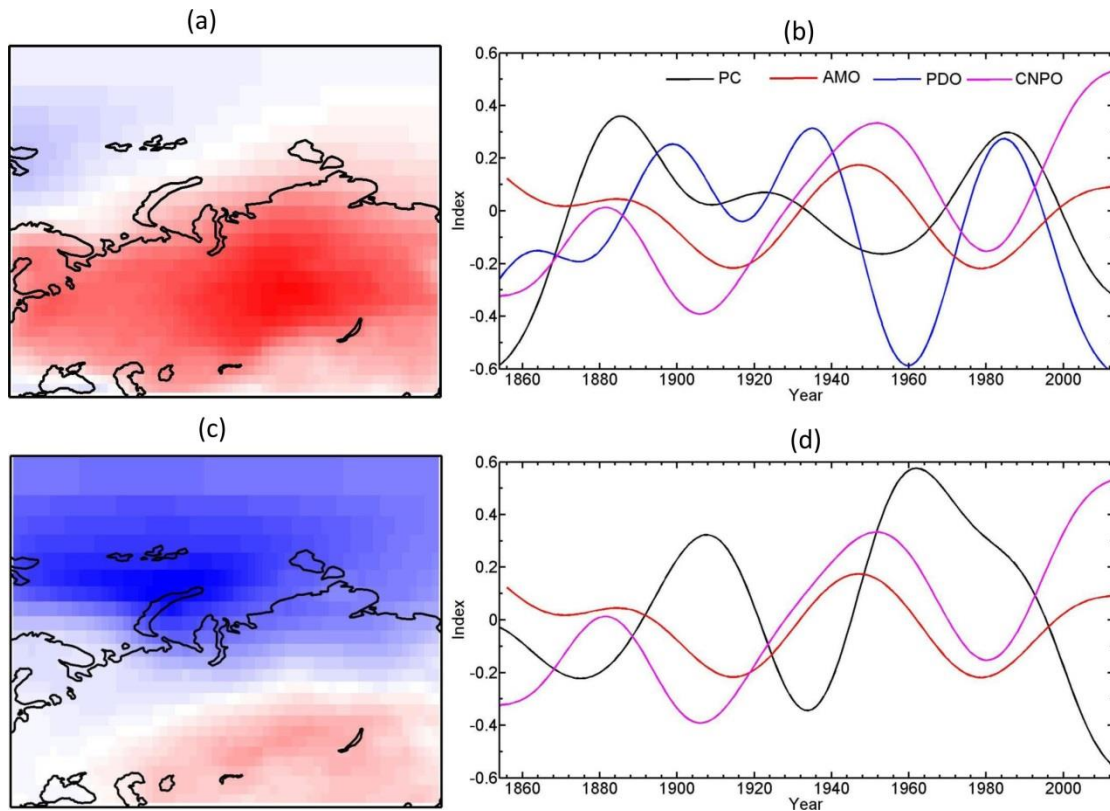
Figure 15. The (a) leading pattern and (b) its time series (PC1 and PC2) of EOF analysis of wintertime surface air temperature anomalies from the 20CR reanalysis for the 1851-2014 period.. Prior to EOF analysis, surface sir temperature data are detrended. A 40-yr low-pass filtered is applied to the time series of PC1, PC2, AMO, PDO, and central North Pacific Ocean (CNPO) indices. The correlation coefficients between PC1 and AMO, PDO and CNPO indices are -0.46 (p<0.0001), 0.38 (p<0.0001), and -0.19 (p=0.019); those between PC2 and and AMO, PDO and CNPO indices are -0.44 (p<0.0001), 0.38 (p<0.0001), and -0.26 (p=0.0009).